



Ab Initio Study of Ground-state CS Photodissociation via Highly Excited Electronic States

Zhongxing Xu¹, Nan Luo², S. R. Federman³, William M. Jackson¹, Cheuk-Yiu Ng¹, Lee-Ping Wang¹, and Kyle N. Crabtree¹

¹ Department of Chemistry, University of California—Davis, One Shields Avenue, Davis, CA 95616, USA; kncrabtree@ucdavis.edu

² Department of Chemical Engineering, University of California—Davis, One Shields Avenue, Davis, CA 95616, USA

³ Department of Physics and Astronomy, University of Toledo, Toledo, OH 43606, USA

Received 2019 April 12; revised 2019 July 10; accepted 2019 July 19; published 2019 September 5

Abstract

Photodissociation by ultraviolet radiation is the key destruction pathway for CS in photon-dominated regions, such as diffuse clouds. However, the large uncertainties of photodissociation cross sections and rates of CS, resulting from a lack of both laboratory experiments and theoretical calculations, limit the accuracy of calculated abundances of S-bearing molecules by modern astrochemical models. Here we show a detailed ab initio study of CS photodissociation. Accurate potential energy curves of CS electronic states were obtained by choosing an active space CAS(8,10) in MRCI+Q/aug-cc-pV(5+d)Z calculation with additional diffuse functions, with a focus on the B and $C^1\Sigma^+$ states. Cross sections for both direct photodissociation and predissociation from the vibronic ground state were calculated by applying the coupled-channel method. We found that the $C - X(0 - 0)$ transition has extremely strong absorption due to a large transition dipole moment in the Franck–Condon region, and the upper state is resonant with several triplet states via spin–orbit couplings, resulting in predissociation to the main atomic products $C(^3P)$ and $S(^1D)$. Our new calculations show that the photodissociation rate under the standard interstellar radiation field is $2.9 \times 10^{-9} \text{ s}^{-1}$, with a 57% contribution from $C - X(0 - 0)$ transition. This value is larger than that adopted by the Leiden photodissociation and photoionization database by a factor of 3.0. Our accurate ab initio calculations will allow more secure determination of S-bearing molecules in astrochemical models.

Key words: astrochemistry – molecular data – molecular processes

Supporting material: machine-readable tables

1. Introduction

Sulfur is an abundant element in space, e.g., the relative abundance of S to H is 1.3×10^{-5} in the solar system (Asplund et al. 2009), and the abundances of S-bearing molecules are sensitive to the physical conditions of their environments. In the interstellar medium (ISM), S-bearing molecules are commonly detected and used as tracers of physical properties (Semenov et al. 2018). In star-forming regions, it has been suggested that abundances of H_2S , SO, and SO_2 could act as a chemical clock on the timescale of 10^4 yr due to both thermal heating and shock interactions (van der Tak et al. 2003; Wakelam et al. 2011). In protoplanetary disks, the abundances of S-bearing species may correlate with the C/O ratio, surface diffusivity, turbulent mixing, X-ray luminosity, ultraviolet (UV) intensity, and grain growth (Semenov et al. 2018).

However, the abundances of S-bearing species are poorly reproduced by modern astrochemical models (Lucas & Liszt 2002), possibly because of the large uncertainties in kinetic data, missing reaction pathways, and unaccounted reservoirs of sulfur (Druard & Wakelam 2012; Loison et al. 2012; Vidal et al. 2017). CS was the first sulfur-bearing molecule observed in interstellar space, initially detected by its 3–2 rotational emission line at 146.969 GHz in several dense sources (Penzias et al. 1971). It has since been found in a wide set of diffuse and dense interstellar clouds (Zuckerman et al. 1972; Drdla et al. 1989; Heithausen et al. 1998; McQuinn et al. 2002; Scappini et al. 2007), as well as comets (Jackson et al. 1982; Canaves et al. 2007). Additionally, CS is the key species in the sulfur chemistry of protoplanetary disks. Observations of the CS column density

are used to determine upper limits for other S-bearing molecules because CS is the only detected sulfur species in many disks, such as DM Tau (Semenov et al. 2018).

In photon-dominated or photodissociation regions (PDRs), UV photons play a critical role in the gas-phase chemistry and act as the most important source of energy. In a general sense, PDRs include peripheries of molecular clouds, diffuse clouds, translucent clouds, the surfaces of protoplanetary disks, and cometary and exoplanetary atmospheres. For small molecules like CS, photodissociation is the key destruction pathway in these environments. Accurate chemical modeling requires wavelength-dependent photoabsorption/photodissociation cross sections at energies above the dissociation limit.

While the ground $X^1\Sigma^+$ and several low-lying electronic states ($a^3\Pi$, $a'^3\Sigma^+$, $d^3\Delta$, $e^3\Sigma^-$, $A^1\Pi$, and $A'^1\Sigma^+$) of CS have been extensively studied by both experiments and ab initio calculations (Shi et al. 2013), very few studies have been done on highly excited states in vacuum UV (VUV) region where CS may undergo photodissociation. The pioneering study on highly excited states of CS was reported by Crawford & Shurcliff (1934), who assigned a strong band system around 251 nm to CS in the emission spectrum of a low-pressure discharge of CS_2 . Later, Donovan et al. (1970) recorded the first VUV spectrum of CS via time-resolved flash photolysis of CS_2 coupled with a high-resolution spectrograph. A strong band observed at 154.1 nm was assigned as $B^1\Sigma^+ - X^1\Sigma^+$ by analogy with the valence isoelectronic species CO, which suggests that the B state of CS has a Rydberg nature like the corresponding state of CO. Two more strong bands at 140.2

Table 1
Exponents of Diffuse Gaussian Functions Added to the aug-cc-pV(5+d)Z Basis Set

C					S		
3s	3p	3d	4s	4p	3d	4s	4p
0.01725	0.01575	0.02850	0.01045	0.00931	0.02850	0.01725	0.02949
		0.01125	0.00413	0.00368	0.01125		0.01500

and 139.9 nm were assigned as the $C \ ^1\Sigma^+ - X \ ^1\Sigma^+ (0 - 0)$ and $(1 - 1)$ transitions, also by analogy with CO.

A subsequent high-resolution VUV absorption study of CS by Stark et al. (1987) confirmed the $C - X$ band assignment and also found additional vibrational components of the $B - X$ transition. Their rotational contour analysis of the $B - X (1 - 0)$ band found that the spectroscopic constants of B state are close to those of the CS^+ ground state, strongly supporting the proposed Rydberg nature of the B state. A rough measurement showed that the line width of the $(1 - 0)$ band is on the order of 1 cm^{-1} , which is clearly broadened by predissociation. All other bands were too diffuse to show rotational structures. Both the $C - X (0 - 0)$ and $(1 - 1)$ bands were diffuse and intense, indicating that the Franck-Condon factors of this transition must notably favor the $(0 - 0)$ transition. The experimental assignments were supported by an early SCF-CI calculation (Bruna et al. 1975), which found that the B and C Rydberg states agreed with experimental energies within 0.1 eV. The spectroscopic evidence suggests that the $B - X$ and $C - X$ bands should play important roles in CS photodissociation in space owing to their strong intensities and their broadening by predissociation. However, at present, the best estimates of the CS photodissociation cross sections in the Leiden database (Heays et al. 2017) were made by combining the measured $B - X$ transition wavelength and vertical excitation energies of higher valence and Rydberg states, and are estimated to be uncertain to a factor of 10.

To improve the accuracy of photodissociation data for astronomical models, further experiments and high-level quantum chemical calculations are needed. Most recently, Pattillo et al. (2018) performed the first high-level ab initio calculations targeting states involved in CS photodissociation. They concluded that the dominant contribution to CS photodissociation from the ground electronic state comes from direct excitation of several dissociative states, including $A' \ ^1\Sigma^+$ and several $^1\Pi$ states, while predissociation via the B state is unimportant. However, their results show significant discrepancies with the experimental VUV spectroscopy of the $^1\Sigma^+$ states: specifically, the energy of the B state is about 7000 cm^{-1} higher than the experimental value and the shape of its potential energy curve (PEC) indicates a much lower vibrational constant compared with experiments, and the C state is missing entirely. Thus, the conclusion that predissociation in highly excited states is unimportant should be reexamined more carefully.

Here, we present a high-level ab initio study of CS photodissociation, including for the first time a detailed investigation of its predissociation via the $B \ ^1\Sigma^+$ and $C \ ^1\Sigma^+$ states. We found that under the Draine radiation field (Draine 1978), inclusion of the $C - X$ and $B - X$ transitions increases the CS photodissociation rate by nearly an order of magnitude compared with the results of Pattillo et al. (2018), and yields an overall rate that is higher by a factor of 3 compared with the Leiden database (Heays et al. 2017). The

details of our theoretical methods are introduced in Section 2. The computed PECs, transition dipole moments (TDMs), photodissociation cross sections, and photodissociation rates are discussed in Section 3, which also presents the comparison between our calculations and experiments. Finally, a summary of the work and its future directions are given in Section 4.

2. Theory and Calculations

2.1. Ab Initio Calculation

Our calculations use the state-averaged complete active space self-consistent field (SA-CASSCF) approach (Knowles & Werner 1985; Werner & Knowles 1985), followed by internally contracted multireference configuration interaction with single and double excitations and the Davidson correction (MRCI+Q) (Knowles & Werner 1988, 1992; Werner & Knowles 1988), a widely used method for calculating excited electronic states, especially for diatomic molecules. We used the quantum chemical package MOLPRO 2015.1 (Werner et al. 2012, 2015) to calculate the adiabatic PECs and TDMs of CS.

To determine the PECs accurately, up to a total of 105 single-point calculations with internuclear separation between 0.78 and 7.93 Å were carried out, with step sizes ranging from 0.0026 to 0.26 Å. The smaller step sizes were used near the equilibrium geometry of the ground state and in the vicinity of several important avoided crossings between states with the same symmetry to ensure good accuracy of calculated properties. We used Dunning's augmented correlation-consistent polarized valence quintuple-zeta Gaussian basis set with tight d orbitals for sulfur [aug-cc-pV(5+d)Z or AV(5+d)z] (Kendall et al. 1992; Dunning et al. 2001). The tight d orbitals have been shown to be essential for calculating accurate properties of S-bearing species (Trabelsi et al. 2018). Several additional diffuse Gaussian functions corresponding to Rydberg atomic orbitals (AOs) of C and S were added to the basis sets to more accurately represent the Rydberg character of the B and C states. Their exponents, derived from Dunning & Hay (1977), are given in Table 1.

MOLPRO is unable to take advantage of the full symmetry of non-Abelian groups (in this case, $C_{\infty v}$), so the calculation is performed in the largest Abelian subgroup (C_{2v}). The reducing map of irreducible representations from $C_{\infty v}$ to C_{2v} is $\Sigma^+ \rightarrow A_1$, $\Sigma^- \rightarrow A_2$, $\Pi \rightarrow (B_1, B_2)$, and $\Delta \rightarrow (A_1, A_2)$. We adopt MOLPRO's order of irreducible representations for C_{2v} to indicate the number of molecular orbitals (MOs) of each symmetry in the following discussion, (a_1, b_1, b_2, a_2) .

The dominant electron configuration of CS in its ground ($X \ ^1\Sigma^+$) state at its equilibrium geometry is $1\sigma^2 2\sigma^2 3\sigma^2 4\sigma^2 5\sigma^2 6\sigma^2 7\sigma^2 1\pi^4 2\pi^4$. To construct the active space for our SA-CASSCF/MRCI+Q calculation, 17 MOs (11, 3, 3, 0) were involved in total. The 7 MOs (5, 1, 1, 0) with lowest energies are kept closed (doubly occupied) in the reference space, while the remaining eight electrons are distributed in the

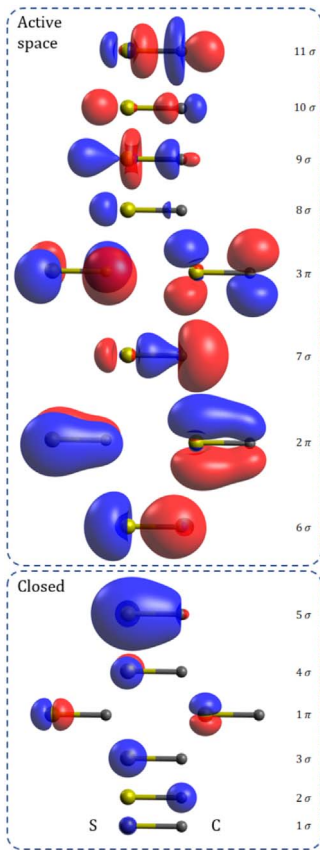


Figure 1. Molecular orbitals (MOs) of CS calculated by SA-CASSCF at 1.54 Å, plotted with isovalue 0.08, except that 0.02 is used for the 1σ MO. Contributions from h type orbitals are excluded from this image owing to limitations of the visualization software. In C_{2v} , σ orbitals correspond to a_1 and π orbitals to the pair (b_1 , b_2). The MOs are listed according to increasing energy, but not to scale. The orbital shapes depend strongly on internuclear distance.

other 10 MOs, forming an active space CAS(8,10) (6, 2, 2, 0). A more detailed discussion of our choice of active space is given in Section 3.1.1. The MOs included in our calculation described above are shown near the equilibrium geometry of the ground state in Figure 1.

The ground states of atomic carbon and sulfur are both 3P , followed by an excited state 1D . The lowest four dissociation limits of CS therefore correlate to $C(^3P_{0,1,2}) + S(^3P_{0,1,2})$, $C(^3P_{0,1,2}) + S(^1D)$, $C(^1D) + S(^3P_{0,1,2})$, and $C(^1D) + S(^1D)$. These combinations give rise to 82 electronic states in C_{2v} symmetry, which are 10^1A_1 , 8^1B_1 , 8^1B_2 , 8^1A_2 , 9^3A_1 , 10^3B_1 , 10^3B_2 , 10^3A_2 , 3^5A_1 , 2^5B_1 , 2^5B_2 , and 2^5A_2 states. We carried out the averaging process among the 82 lowest-energy states of these C_{2v} symmetries in the SA-CASSCF calculations regardless of which symmetries they correspond to in $C_{\infty v}$; this changes with internuclear distance.

The orbitals optimized by SA-CASSCF are used in the MRCI+Q calculations. The CI treatment was carried out by employing a reference space of 2053 (1A_1), 1843 (3A_1), 1672 (1B_1 and 3B_1), 1368 (1A_2 and 3A_2), 891 (5A_1), 1000 (5B_1), and 1144 (5A_2) configurations, from which all single and double excitations were generated. As a demonstration of the calculation size, the total number of uncontracted configurations was 502,853,808 while the total number of contracted configurations was 17,569,850 in 1A_1 symmetry for the MRCI+Q calculation at

1.54 Å. The exact number of configurations varies with internuclear distance, spatial symmetry, and spin multiplicity. The Davidson correction with relaxed references was added to the MRCI energies. TDMs are obtained at the level of MRCI.

For several bound states with obvious potential wells, we calculated the spectroscopic constants from the PECs for comparison with previous calculations and experimental data. First, we obtained the rovibrational energy levels by solving the one-dimensional Schrödinger equation numerically using the DUO program (Yurchenko et al. 2016). Then the spectroscopic constants, including T_e , ω_e , $\omega_e x_e$, B_e , and α_e , were determined by fitting the energy levels of the first 10 vibrational states.

2.2. Photodissociation Cross Sections

Photodissociation may occur through one of two main pathways. Absorption into an unbound excited electronic state results in direct dissociation, and is characterized by a broad, weak cross section. Indirect photodissociation, on the other hand, begins by absorption into a bound excited state, followed by predissociation: nonradiative coupling into a nearby unbound state. Cross sections for indirect photodissociation show resolved or partially resolved rovibrational transitions associated with the upper electronic state that are lifetime broadened. When the predissociation timescale is fast compared with other relaxation mechanisms (e.g., spontaneous emission), nearly every absorption event leads to dissociation.

The coupled-channel Schrödinger equation (CSE) technique is employed here to study the predissociation mechanisms of CS $^1\Sigma^+$ states. When solving the Schrödinger equation, there are two ways to describe the coupled system of nuclei and electrons. The electronic states calculated by the ab initio methods above are in the adiabatic representation, where the electronic Hamiltonian is diagonalized precisely and the couplings between states arise from a nuclear kinetic energy operator. An alternative method uses the diabatic representation, where the nuclear kinetic energy coupling terms are minimized while introducing new couplings that are treated as interactions between different electronic states. The diabatic states approximately follow the same electronic character as a function of internuclear distance, while the adiabatic states' electronic character varies. In principle, these two representations are equivalent after introducing the appropriate coupling terms. For convenience, the diabatic representation is used in this study because the couplings in adiabatic states vary strongly with internuclear distance, which creates difficulties in modeling the predissociation process.

In the CSE method, the complete coupled-wavefunction $\psi_i(\mathbf{r}, R)$ is expressed as a linear combination of a set of N_T diabatic (or adiabatic) electronic rotational states $\phi_j(\mathbf{r}; R)$, which are also called coupled channels,

$$\psi_i(\mathbf{r}, R) = \sum_{j=1}^{N_T} \frac{1}{R} \chi_{ij}(R) \phi_j(\mathbf{r}; R), \quad (1)$$

where R is the internuclear distance, and $\chi_{ij}(R)$ represent R -dependent expansion coefficients between states $\phi_j(\mathbf{r}; R)$. For a given energy E , the Schrödinger equation for the radial wavefunctions can be written as

$$\frac{\partial^2}{\partial R^2} \chi(R) = -\frac{2\mu}{\hbar^2} \chi(R) [EI - V(R)], \quad (2)$$

where μ is the reduced mass of the molecule, I is the identity matrix, and $V(R)$ is the interaction matrix, which is composed of PECs as diagonal elements and coupling terms (such as non-adiabatic coupling and spin-orbit coupling (SOC)) as off-diagonal elements.

The SOCs and non-adiabatic couplings are calculated by MOLPRO. The SOCs for MRCI wavefunctions are calculated by using the full Breit-Pauli operator between internal configurations, while contributions of external configurations are calculated by a mean-field one-electron Fock operator. For adiabatic states, the non-adiabatic coupling matrix elements (NACMEs) are computed by finite differences of the MRCI wavefunctions. Details about building the interaction matrix, including obtaining diabatic representations, are discussed further in Section 3.2. Equation (2) is solved numerically to give the coupled wavefunctions for mixed upper states.

Assuming alternate decay pathways such as spontaneous emission or collisional relaxation are slow, the total photodissociation cross section from an initial state with J'' is obtained by summing over all open channels γ and all allowed J' (Heays 2010),

$$\sigma_g(\tilde{\nu}) = \sum_{J'} \sum_{\gamma} \left[\frac{\pi \tilde{\nu}}{3 \hbar \epsilon_0} \frac{g}{2J'' + 1} \sum_k (|\langle \chi_{\gamma k} | M | \chi_g \rangle|^2 S_{J''}^{\Delta J}) \right], \quad (3)$$

where $\tilde{\nu}$ is the photon energy in wavenumbers, M is the R-dependent electric-dipole transition moment between the unmixed lower (ground) state with radial wavefunction χ_g and each upper state k with mixed wavefunction $\chi_{\gamma k}$ coupled to open channel γ . The Hönl-London factors $S_{J''}^{\Delta J}$ (Hansson & Watson 2005; Watson 2008), which indicate the relationship between the total intensity of a vibronic band and the rotational quantum numbers, can be expressed for these types of transitions as

$${}^1\Sigma^+ - {}^1\Sigma^+ : \quad \begin{aligned} S_{J''}^P &= J'' \\ S_{J''}^R &= J'' + 1 \end{aligned} \quad (4)$$

$${}^1\Pi - {}^1\Sigma^+ : \quad \begin{aligned} S_{J''}^P &= (J'' - 1)/2 \\ S_{J''}^Q &= (2J'' + 1)/2 \\ S_{J''}^R &= (J'' + 2)/2 \end{aligned} \quad (5)$$

for $P(\Delta J = -1)$, $Q(\Delta J = 0)$, and $R(\Delta J = +1)$ branches. In our case, the degeneracy factor g is 1 for a ${}^1\Sigma^+ - {}^1\Sigma^+$ transition and 2 for a ${}^1\Pi - {}^1\Sigma^+$ transition.

For a particular transition, the line width can be used to estimate the predissociation timescale τ_{pd} and compared with the spontaneous emission and collision timescales (τ_{se} and τ_{coll}). If $\tau_{pd} \ll \tau_{se}$ and τ_{coll} , then the calculated cross sections are good estimates of the photodissociation cross section. Otherwise, a time-dependent method should be applied or a tunneling probability η should be included for correction. As shown below, in the case of CS, the predissociation efficiency is essentially 1.

Direct photodissociation is simply a special case of the CSE model in which only one unmixed upper state can be excited from the ground state. Because the upper state is unbound and certain to dissociate, the calculated result is an exact photodissociation cross section. Thus, the CSE approach simultaneously calculates the direct photodissociation cross sections in addition to those that proceed via predissociation. In

this study, photodissociation cross sections are calculated with PyDiatom (Gibson 2016), which solves the time-independent coupled-channel Schrödinger equation using the Johnson renormalized Numerov method (Johnson 1978).

Using the CSE method, a rotationless ($J' - J'' = 0 - 0$) transition is calculated for the ground X state with $v'' = 0$. We also calculated the photodissociation cross sections for transitions from the ground state with $v'' = 0, 1, 2$ and different J'' . Assuming local thermodynamic equilibrium (LTE), the total photodissociation cross sections at given temperature T are calculated by

$$\sigma(\lambda, T) = \frac{1}{Q} \sum_i \sigma_i(\lambda) g_i e^{-E_i/k_b T}, \quad (6)$$

where Q is the partition function, E_i is the energy of all achievable ground rovibrational states with rotational degeneracy $g_i = 2J'' + 1$, and k_b is Boltzmann's constant.

2.3. Photodissociation Rates in Astrophysical Environments

The photodissociation rate of a molecule in an UV radiation field is

$$k = \int \sigma(\lambda) I(\lambda) d\lambda, \quad (7)$$

where $\sigma(\lambda)$ is the photodissociation cross section and $I(\lambda)$ is the radiation intensity. We compute the photodissociation rate of CS from its ground (X) state with $(v'', J'') = (0, 0)$ in the standard interstellar radiation field (ISRF) given by Draine (1978). The LTE photodissociation rates for different temperatures are also calculated.

3. Results and Discussion

The layout of this section is as follows. The PECs and TDMs obtained from ab initio calculations are given in Section 3.1, including a highlight on the main feature of our calculations. Then, the details about building the coupled-channel model is discussed in Section 3.2. Finally, the dissociation cross sections and rates are presented in Section 3.3.

3.1. Ab Initio Calculation

3.1.1. Optimization of MRCI Calculation

The accuracy of the calculated photodissociation cross sections relies on the PECs and TDMs obtained from the SA-CASSCF/MRCI+Q calculation. The quality of an MRCI+Q calculation is sensitive to the choice of active space and basis set, both of which require careful consideration. Previous theoretical studies of CS excited states (Shi et al. 2013; Pattillo et al. 2018) used the aug-cc-pV6Z (AV6Z) basis set with the active space CAS(10,8) where the number of active orbitals for each irreducible representation is given as (4,2,2,0). The fact that the properties of the B state calculated by Pattillo et al. (2018) disagree with experiments (Donovan et al. 1970; Stark et al. 1987) suggests that this active space is not suitable for accurately calculating highly excited states. One reasonable explanation for the discrepancy is that some dominant configurations of the B state are not included in the reference space because some significantly occupied MOs in these configurations are outside of the active space.

Although there is no golden rule to determine the ideal active space, including more virtual orbitals is generally necessary to

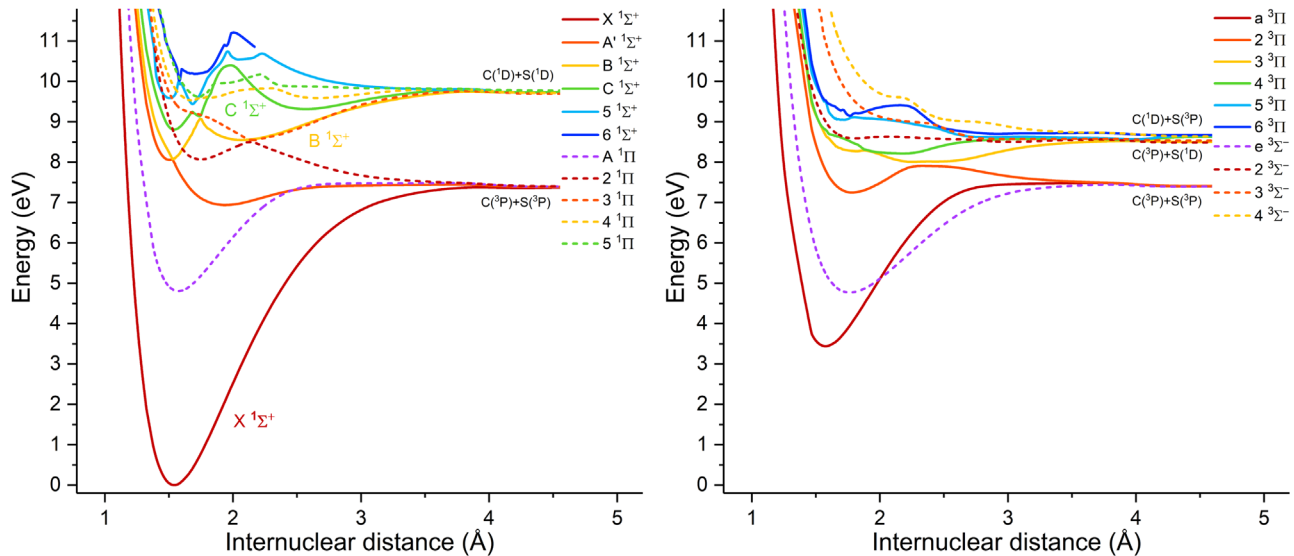


Figure 2. Adiabatic potential energy curves for CS $^1\Sigma^+$, $^1\Pi$ (left), $^3\Pi$, and $^3\Sigma^-$ (right) electronic states.

improve the quality of the calculation, especially for Rydberg states. Both previous spectroscopic experiments and comparison between CO and CS indicate the *B* and *C* states have Rydberg nature, involving high-energy σ -type orbitals. Motivated by these experimental observations, we systematically included more a_1 (i.e., σ) virtual orbitals in the active space, and found that at CAS(10,11) (7,2,2,0) the SA-CASSCF/MRCI+Q calculation was stable over the whole internuclear distance range. Smaller active spaces resulted in a stability problem around 2.0 Å.

As the internuclear distance increases, the dominant electron configuration changes in the adiabatic representation. For the ground $X^1\Sigma^+$ state, this occurs twice, at 2.1 and 2.8 Å, which can roughly be interpreted as the points at which the C = S double bond breaks stepwise. While the change in configuration itself is straightforward to treat, the changes in the shapes of the MOs themselves cause significant stability problems when the active space is too small. With our active space, we were able to achieve continuous and smooth PECs up to at least the $C^1\Sigma^+$ state. Addition of one more σ orbital resulted in a dramatic increase in the single-point calculation time, rendering it impractical for the complete study.

Calculations with smaller basis sets showed that the $5a_1$ MO is doubly occupied in the most important configurations for all states we are able to calculate. Therefore to save calculation time, we put the $5a_1$ MO into the closed-shell space, resulting in our final active space of CAS(8,10) (6,2,2,0).

Because of our large active space, we could not use the aug-cc-pV6Z basis set as in previous studies. Instead, we used the aug-cc-pV(5+d)Z basis set supplemented with additional diffuse orbitals located on both carbon and sulfur atoms. The total number of AOs in our basis is 299 (112,72,72,43). Keeping the 6 lowest MOs (4,1,1,0) as core MOs, in the MRCI+Q calculation for $^1\Sigma^+$ states at 1.54 Å, from the reference space consisting of 2053 configurations, 1.76×10^7 contracted and 5.03×10^8 uncontracted configurations are generated. In comparison, in the aug-cc-pV6Z basis set, there are 382 (134,93,93,62) AOs. To compute the same number of states using the active space CAS(10,8) (4,2,2,0) and the aug-cc-pV6Z basis set, only a total of 1.11×10^7 contracted and 7.00×10^7 uncontracted configurations are produced from the

reference space with 240 configurations. Thus, our large reference space is appropriate for calculating both valence and Rydberg states of CS, and justifies using a slightly smaller, tailored basis set.

As a final point, our choice of active space was focused primarily on accurate calculations of $^1\Sigma^+$ states. It is possible that including more π MOs in the active space, such as using CAS(8,12) (6,3,3,0), would improve the quality of calculation especially for high-lying Π states. However, the large number of configurations we included in the MRCI+Q calculation still promises good accuracy even for non- $^1\Sigma^+$ states. Moreover, the spectroscopic constants calculated for low-lying excited states from our PECs match available experimental data well, which enhances our confidence.

3.1.2. PECs and TDMs

Employing the approaches described in Section 2.1, we have calculated the PECs of 49 states in total, including 7 $^1\Sigma^+$, 3 $^1\Sigma^-$, 7 $^1\Pi$, 4 $^1\Delta$, 4 $^3\Sigma^+$, 5 $^3\Sigma^-$, 8 $^3\Pi$, 5 $^3\Delta$, 2 $^5\Sigma^+$, 1 $^5\Sigma^-$, 2 $^5\Pi$, and 1 $^5\Delta$. Among all these states, the adiabatic PECs of several $^1\Sigma^+$, $^1\Pi$, $^3\Pi$, and $^3\Sigma^-$ states are shown in Figure 2 because they are directly related to the following dissociation study, while all data are available in a machine-readable format in the Appendix with PECs of other states.

The potential energy scale used here is referenced to a zero defined by the potential minimum of the ground state $X^1\Sigma^+$. State names are kept consistent for states already tabulated in the NIST database (Huber & Herzberg 1979). For the ground state and several low-lying excited states, calculated spectroscopic constants are listed in Table 2, along with data from previous theoretical calculations and experiments where available. The dissociation energies D_e are estimated to be the calculated MRCI+Q energies at $R = 7.9$ Å. The error induced by long-range interactions is estimated to be smaller than 0.0010 eV based on the formula and quadrupole-quadrupole coefficients given by Pattillo et al. (2018).

Of the 10 singlet electronic states calculated with A_1 symmetry, 6 correspond to $^1\Sigma^+$ at $R = 2.1$ Å: X , A' , B , C , 5 , and $6^1\Sigma^+$. At $R > 2.2$ Å, the $6^1\Sigma^+$ is no longer among the first 10 A_1 states in C_{2v} . Because the remaining part of its potential

Table 2
Spectroscopic Constants for Low-lying States of CS

State	Method	R_e (Å)	T_e (cm ⁻¹)	ω_e (cm ⁻¹)	$\omega_e x_e$ (cm ⁻¹)	B_e (cm ⁻¹)	$10^3 \alpha_e$ (cm ⁻¹)	D_e^a (eV)
$X^1\Sigma^+$	Calc ^b	1.540	0	1284.1	8.2	0.814	6.0	7.47
	Expt ^c	1.535	0	1285.1	6.5	0.820	5.9	7.43
	Calc ^d	1.533	0	1286.8	4.9	0.822	6.0	7.46
$a^3\Pi$	Calc ^b	1.577	27735.5	1129.9	7.8	0.777	6.9	4.05
	Expt ^e	1.568	27661.0	1135.1	7.7	0.785	7.2	4.00
	Calc ^d	1.569	27721.7	1133.6	7.1	0.786	7.7	4.05
$a'^3\Sigma^+$	Calc ^b	1.737	31411.7	832.1	5.9	0.640	5.5	3.59
	Expt ^f	1.725	31331.4	830.7	5.0	0.649	6.0	3.55
	Calc ^d	1.720	31310.2	829.4	12.9	0.652	9.1	3.59
$d^3\Delta$	Calc ^b	1.753	35585.8	787.0	3.4	0.629	5.6	3.07
	Expt ^f	1.742	35675.0	795.6	4.9	0.637	6.1	3.01
	Calc ^d	1.741	35863.5	795.9	5.3	0.635	7.5	3.04
$e^3\Sigma^-$	Calc ^b	1.767	38470.4	749.8	3.5	0.619	6.2	2.71
	Expt ^g	1.766	38683.	752	4.7	0.619	4.	2.64
	Calc ^d	1.762	38810.6	751.4	4.5	0.622	6.6	2.67
$A^1\Pi$	Calc ^b	1.575	38779.4	1052.4	9.2	0.780	8.9	2.67
	Expt ^g	1.574	38904.4	1073.4	10.1	0.780	6.3	2.61
	Calc ^d	1.565	38943.2	1075.0	9.2	0.784	7.4	2.65
$1^1\Sigma^-$	Calc ^b	1.771	38622.9	744.6	4.8	0.616	6.5	2.69
	Calc ^d	1.767	39398.3	746.7	6.1	0.618	6.4	2.65
$1^1\Delta$	Calc ^b	1.778	39626.9	718.0	3.9	0.611	6.8	2.59
	Calc ^d	1.777	40197.7	723.2	5.7	0.612	6.6	2.54
$A'^1\Sigma^+$	Calc ^b	1.945	55960.2	464.9	3.2	0.511	11.0	0.55
	Expt ^h	1.944	56505	462.4	7.5	0.511	10.9	0.43
	Calc ^d	1.958	57115.3	459.4	1.7	0.496	2.5	0.41
$X^2\Sigma^+$ (CS ⁺)	Calc ^b	1.500	0	1369.8	9.1	0.859	6.3	11.34 ⁱ
	Expt ^j	1.492	0	1376.6	7.8	0.867	6.5	11.32 ^k

Notes.

^a Experimental D_e of $X^1\Sigma^+$ is determined by adding energy of $v = 0$ to $D_0^0 = 7.355$ eV (Coppens & Drowart 1995). Experimental D_e of other states is estimated by $D_e(X^1\Sigma^+)$ and their T_e .

^b This work.

^c Mockler & Bird (1955), Kewley et al. (1963), Lovas & Krupenie (1974), Huber & Herzberg (1979).

^d Shi et al. (2013).

^e Tewarson & Palmer (1968), Taylor et al. (1972), Cossart & Bergeman (1976), Huber & Herzberg (1979).

^f Barrow et al. (1960), Field & Bergeman (1971), Cossart & Bergeman (1976), Huber & Herzberg (1979).

^g Barrow et al. (1960), Huber & Herzberg (1979).

^h Bell et al. (1972).

ⁱ Calculated ionization energy of CS ground X state.

^j Gauyacq & Horani (1978).

^k Experimental ionization energy of CS ground X state (Coppens & Drowart 1995).

is still helpful to construct diabatic states, we include $6^1\Sigma^+$ in Figure 2.

The X state is deeply bound with an equilibrium internuclear distance of 1.540 Å and an estimated dissociation energy 7.47 eV. The calculated spectroscopic constants, especially the vibrational constant ω_e , are in excellent agreement with experimental data (Table 2). Next is the A' state, which is weakly bound with a much longer equilibrium bond distance, reflecting the fact that its main configuration has one electron excited from a bonding valence MO to an antibonding MO. The B state has two potential wells. The first, at 1.53 Å, lies near an avoided crossing with the A' state, while the second is at 2.06 Å. The C state has its potential minimum at 1.54 Å, which is nearly identical to that of the X state. The shape of the C state, which is about 0.35 eV higher than its

equilibrium point, is affected by avoided crossings with the B and $5^1\Sigma^+$ states. Following a maximum at 1.95 Å, a second weak potential well appears. For both the B and C states, the potential well near 1.50 Å corresponds to a Rydberg configuration, while the second well toward larger distances corresponds to a valence-bound electron configuration. A more detailed discussion of the spectroscopic properties of the B and C states can be found in Section 3.3. The 5 and 6 $^1\Sigma^+$ states have complicated potential curves, possibly arising from avoided crossings with still higher states.

The five $^1\Pi$ states are shown in Figure 2. The $A^1\Pi$ state has a calculated equilibrium internuclear distance of 1.575 Å with potential minimum of 38,779.4 cm⁻¹, which is only 125 cm⁻¹ lower than the experimental value. The calculated harmonic

vibrational constant is 21 cm^{-1} smaller than the experimental value of 1073.4 cm^{-1} . No experimental data are available to compare with the higher-lying $^1\Pi$ states. Our calculations indicate that the 2 and 3 $^1\Pi$ states have a prominent avoided crossing around 2.1 \AA . Finally, the 4 and 5 $^1\Pi$ states lie close in energy and have unusual shapes, indicating significant Rydberg-valence mixing. The $E \ ^1\Pi$ state identified in the spectrum of Donovan et al. (1970) may be composed of a combination of the 2, 3, 4, and 5 adiabatic states in a diabatic representation. However, as discussed in more detail later, construction of such a complex diabatic state is complicated, and we did not pursue this further.

The $1 \ ^1\Sigma^-$ state has a potential minimum of $38,622.9 \text{ cm}^{-1}$ at $R = 1.771 \text{ \AA}$, while the $1 \ ^1\Delta$ state has a calculated equilibrium internuclear distance of 1.778 \AA with a potential minimum of $39,626.9 \text{ cm}^{-1}$. They are almost degenerate, indicating that they share similar configurations. Because direct excitation from the ground state is forbidden, no experimental data are available for comparison. Our T_e values are about 800 and 600 cm^{-1} lower than those fitted by Shi et al. (2013) for the $1 \ ^1\Sigma^-$ and $1 \ ^1\Delta$ states, respectively, and our calculated R_e values are in good agreement with theirs. The 2 $^1\Sigma^-$ and 2, 3, and 4 $^1\Delta$ states are either unbound or very weakly bound, converging to the $C \ (^1D) + S \ (^1D)$ atomic limit.

The remaining electronic states of CS that correlate to one of the four lowest-energy atomic limits are triplet and quintet states. Quintet states are not involved in the photodissociation of ground-state CS and are not discussed further. Triplet states, however, may play an important role in the predissociation of $1 \ ^1\Sigma^+$ states via the spin-orbit interaction, as suggested by Donovan et al. (1970), even though direct excitation is forbidden from the ground state. The main features of the triplet state PECs from our calculations are briefly summarized here.

The $a \ ^3\Sigma^+$ state has an equilibrium distance of 1.737 \AA with a potential minimum $31,411.7 \text{ cm}^{-1}$, which is only about 80 cm^{-1} larger than the experimental value. The 2 and 3 $^3\Sigma^+$ states have an avoided crossing at 1.98 \AA , and the local maximum at 1.77 \AA of the 3 $^3\Sigma^+$ state represents a Rydberg-valence mixing.

Next, the $e \ ^3\Sigma^-$ state has a potential minimum of $38,470.4 \text{ cm}^{-1}$ at $R = 1.767 \text{ \AA}$, and its calculated spectroscopic constants agree well with experimental data. Higher-energy $^3\Sigma^-$ states are unbound and converge to either the $C \ (^3P) + S \ (^1D)$ or $C \ (^1D) + S \ (^3P)$ atomic limits.

The $a \ ^3\Pi$ state has the potential minimum of $27,735.5 \text{ cm}^{-1}$ at $R = 1.577 \text{ \AA}$, and its calculated vibrational constant is 1129.9 cm^{-1} , only 5.2 cm^{-1} smaller than the experimental value. An avoided crossing between the 2 and 3 $^3\Pi$ states spans $R = 2.25$ to 2.50 \AA , and another one between the 3 and 4 $^3\Pi$ states lies at $R = 1.94 \text{ \AA}$. The PECs of higher $^3\Pi$ states are close to each other, with complicated potential structures.

Finally, the $d \ ^3\Delta$ state has an equilibrium bond length of 1.753 \AA with a potential energy minimum of $35,585.8 \text{ cm}^{-1}$. The fitted spectroscopic constants are in good agreement with those obtained by experiments. Higher $^3\Delta$ states are either unbound or have shallow potential wells.

Of all these states, only those of $^1\Sigma^+$ and $^1\Pi$ symmetry are directly accessible from the ground X state by radiative transitions, according to the selection rules for heteronuclear

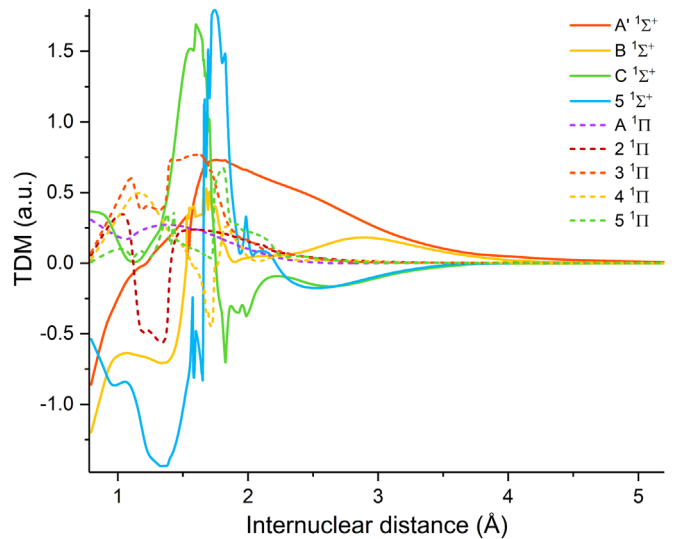


Figure 3. Transition dipole moments between the ground electronic state of CS and each excited state.

diatomic molecules in Hund's case (a) and (b),

$$\Delta\Lambda = 0, \pm 1; \quad \Delta S = 0; \quad + \leftrightarrow - . \quad (8)$$

Thus, they are expected to play the most important role in the photodissociation of CS in astronomical environments. TDMs from the ground X state to excited $^1\Sigma^+$ and $^1\Pi$ states are shown in Figure 3. We find that the C and $5 \ ^1\Sigma^+$ states have much larger TDMs compared with all other states. Most importantly, the TDM of the C state is 1.5 a.u. at 1.54 \AA , which is the equilibrium internuclear distance for both the X and $C \ ^1\Sigma^+$ states. This indicates that the $C - X \ (0 - 0)$ transition should be extremely strong, which agrees with the experimental VUV absorption spectra of Donovan et al. (1970) and Stark et al. (1987). Of the $^1\Pi$ states, $3 \ ^1\Pi$ has the largest TDM, which is about 0.7 a.u.

To verify our TDM calculations, we determined f -values for the $A - X$ system for comparison with available experimental and theoretical results (e.g., Carlson et al. 1979; Mahon et al. 1997; Ornellas 1998; Li et al. 2013). The suite of oscillator strengths is in excellent agreement. A selection of representative values appears in Table 3.

In their tentative detection of the CS $C - X$ band in diffuse molecular gas, Destree et al. (2009) required estimates of the oscillator strength to derive the column density. To do this, they adopted an f -value of 0.14 for the $C - X \ (0 - 0)$ band based on that for the isovalent molecule CO (Federman et al. 2001). However, our calculations yield a significantly larger f -value of 0.45 owing to the large TDM for CS. With the larger CS f -value derived here, the column density inferred from the astronomical observations is substantially reduced; consequently, the expected amount of absorption of the $A - X \ (0 - 0)$ transition at 257.7 nm ($f = 0.096$) is also much lower, and well below the upper limit available from the astronomical measurements.

3.2. Coupled-channel Model

Several of the high-energy PECs feature avoided crossings, and in particular the B and C states are likely to share resonant levels with unbound states and therefore may decay by

Table 3
Calculated f -values for the $A - X$ System

Band ($v' - v''$)	$f_{v'v''} (\times 10^2)$			Band ($v' - v''$)	$f_{v'v''} (\times 10^2)$			Band ($v' - v''$)	$f_{v'v''} (\times 10^2)$		
	This Work	Expt ^a	Theory ^b		This Work	Expt ^a	Theory ^b		This Work	Expt ^a	Theory ^b
(0 - 0)	1.19	0.96	1.16	(2 - 0)	0.02	0.02	0.03	(4 - 0)	0.00	...	0.00
(0 - 1)	0.17	0.12	0.16	(2 - 1)	0.45	0.35	0.47	(4 - 1)	0.01	...	0.01
(0 - 2)	0.02	0.01	0.02	(2 - 2)	0.40	0.35	0.34	(4 - 2)	0.15	0.12	0.19
(0 - 3)	0.00	...	0.00	(2 - 3)	0.30	0.24	0.29	(4 - 3)	0.56	0.45	0.53
(0 - 4)	0.00	...	0.00	(2 - 4)	0.08	0.06	0.08	(4 - 4)	0.03	0.03	0.01
(0 - 5)	0.00	...	0.00	(2 - 5)	0.01	...	0.01	(4 - 5)	0.23	...	0.19
(1 - 0)	0.27	0.20	0.28	(3 - 0)	0.00	...	0.00	(5 - 0)	0.00	...	0.00
(1 - 1)	0.74	0.63	0.69	(3 - 1)	0.08	0.06	0.10	(5 - 1)	0.00	...	0.00
(1 - 2)	0.27	0.20	0.26	(3 - 2)	0.55	0.44	0.56	(5 - 2)	0.02	0.02	0.03
(1 - 3)	0.05	0.03	0.04	(3 - 3)	0.17	0.15	0.11	(5 - 3)	0.25	0.20	0.29
(1 - 4)	0.00	...	0.00	(3 - 4)	0.29	0.24	0.26	(5 - 4)	0.48	0.39	0.41
(1 - 5)	0.00	...	0.00	(3 - 5)	0.12	...	0.11	(5 - 5)	0.00	...	0.01

Notes.

^a Derived from lifetime measurements of R -branch band heads with an inherent $\sim 10\%$ uncertainty in general (Carlson et al. 1979).

^b Calculated by CASSCF/MRCI (Ornellas 1998).

predissociation. Because the typical timescale for predissociation is much faster than spontaneous emission for small diatomic molecules, it is normally reasonable to treat their dissociation efficiency, η_d , as unity in a collision-free environment. All photoabsorption is therefore expected to lead to dissociation (Heays et al. 2017). Experimental line broadening observed in the $B - X$ and $C - X$ bands supports the fast predissociation of CS (Donovan et al. 1970; Stark et al. 1987). In this study, we use the CSE method to investigate the predissociation of CS in detail.

The CSE approach has been described by van Dishoeck et al. (1984) and Heays (2010). It has previously been used to study predissociation of other diatomic molecules, including N_2 (Heays et al. 2015), O_2 (Gibson & Lewis 1996; Lewis et al. 2001), and S_2 (Lewis et al. 2018), yielding good agreement between computed and experimental cross sections. In these studies, diabatic PECs are typically constructed from experimentally measured rovibrational energy levels using, for instance, the Rydberg–Klein–Rees (RKR) method. Then, the coupling terms and TDMs are fitted iteratively by comparing the calculated cross sections, resonance positions, and widths with measured values. However, for many of the important predissociative states of CS, the available spectroscopic data for CS are insufficient to allow such methods. We aim to obtain the photodissociation cross sections from pure ab initio calculations.

Building the coupled-channel model consists of constructing the interaction matrix $V(R)$, whose diagonal elements are diabatic PECs, and off-diagonal elements represent couplings between states. The wavefunctions of the coupled states are obtained from the interaction matrix and are used to derive the cross sections. It is impractical to include all states in the model because of the high density of states with energies above 8 eV. Motivated by the strong absorption bands observed by Donovan et al. (1970) and Stark et al. (1987), our model focuses primarily on treating predissociation originating in the B and C states.

We constructed diabatic PECs of the A' , B , C , and $3' \ ^1\Sigma^+$ states from the adiabatic ones (Lefebvre-Brion & Field 2004). Although it is theoretically possible to diabaticize the PECs by applying the adiabatic-to-diabatic transformation matrix, which

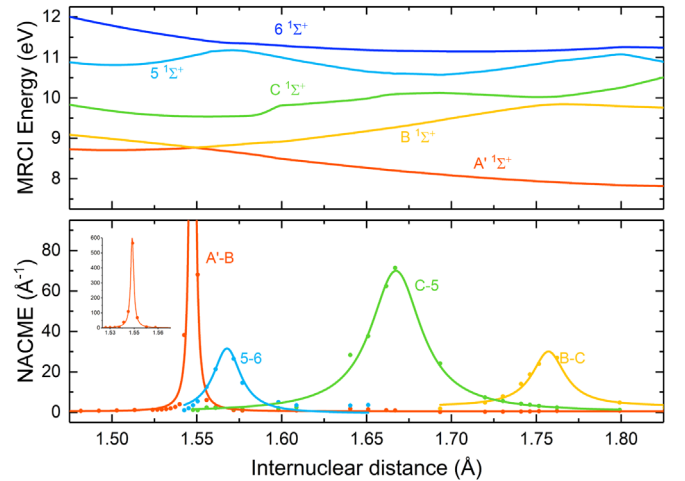


Figure 4. Adiabatic MRCI/aug-cc-5V(5+d)Z PECs for excited $^1\Sigma^+$ states (without the Davidson correction), along with their calculated NACMEs.

can be calculated from the NACMEs (Baer 2006), we did not use this method for three main reasons. First, calculation of the matrix at each internuclear distance requires an integral of the NACME from infinite separation. Small errors in each NACME may accumulate during the integration and yield artificial PECs. Second, solving the matrix is difficult for a system larger than two states, and the procedure is even more complicated in this case because the crossings between B , C , and $5 \ ^1\Sigma^+$ states are close. Moreover, the NACMEs are calculated only at the MRCI level, corresponding to MRCI energies shown in Figure 4. The MRCI+Q energies, which include the Davidson correction, are more accurate and smoother. Instead, we diabaticized the states by exchanging the adiabatic MRCI+Q energies on both sides of the crossing ranges and connecting the PEC segments linearly. For B and C states beyond our data region, we extended their PECs according to the shape of MRCI+Q PEC of CS^+ calculated with the same basis set and active space.

Initial values for the R -independent diabatic coupling matrix elements, H^e , are estimated to be half the energy gaps at the crossing points shown in Figure 2 (Lefebvre-Brion & Field 2004).

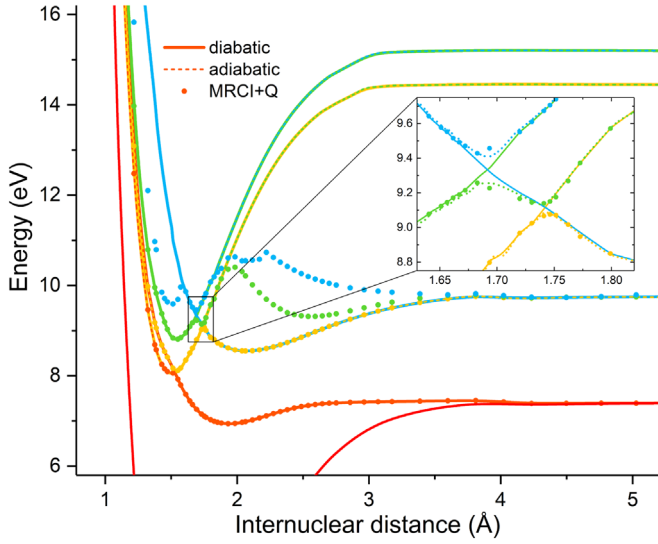


Figure 5. $^1\Sigma^+$ states of CS: MRCI+Q ab initio energies, constructed diabatic PECs, and their corresponding adiabatic PECs obtained by diagonalizing the diabatic interaction matrix $V(R)$.

For example, the diabatic coupling between the B and $3'$ states corresponds to the coupling between the B and C states in the adiabatic representation. The B and $3'$ diabatic potentials cross at 1.74 \AA , with an MRCI+Q energy difference of 566 cm^{-1} between B and C diabatic states, yielding an estimate for $H^e(B, 3')$ of 283 cm^{-1} .

We explored another method to estimate the diabatic coupling matrix elements without numerical integration (Lefebvre-Brion & Field 2004). Normally it can be assumed that the energy differences between two diabatic potentials, $E_1^d(R)$ and $E_2^d(R)$, vary linearly with internuclear distance R in the crossing region

$$E_1^d(R) - E_2^d(R) = a(R - R_c), \quad (9)$$

where R_c is the crossing point of these two potentials and a is the linear coefficient. Then the shape of the NACME forms a Lorentzian peak near R_c with a full width at half-maximum (FWHM) of $4H^e/a$:

$$\left\langle \psi_1^{ad} \left| \frac{\partial}{\partial R} \right| \psi_2^{ad} \right\rangle_R = \frac{H^e/a}{4(H^e/a)^2 + (R - R_c)^2}. \quad (10)$$

Thus, H^e can be estimated by

$$H^e = \frac{a \times \text{FWHM}}{4}. \quad (11)$$

The NACMEs between adiabatic states calculated by MOLPRO do not include the Davidson correction (+Q); their values and the corresponding MRCI energies are shown in Figure 4. A higher and narrower NACME peak between adiabatic states means weaker coupling between the diabatic states. For the example mentioned above, a is calculated to be 11.4 eV/\AA and the FWHM is 0.036 \AA , which results in $H^e = 827 \text{ cm}^{-1}$. This number disagrees with the above value of 283 cm^{-1} . Instead, it matches the half-energy gap 788 cm^{-1} at the crossing point at 1.75 \AA in the MRCI PEC, shown in Figure 4. This latter approach fails because the Davidson correction contributes significantly to the energies of the excited states, especially near the avoided crossings in the MRCI calculation.

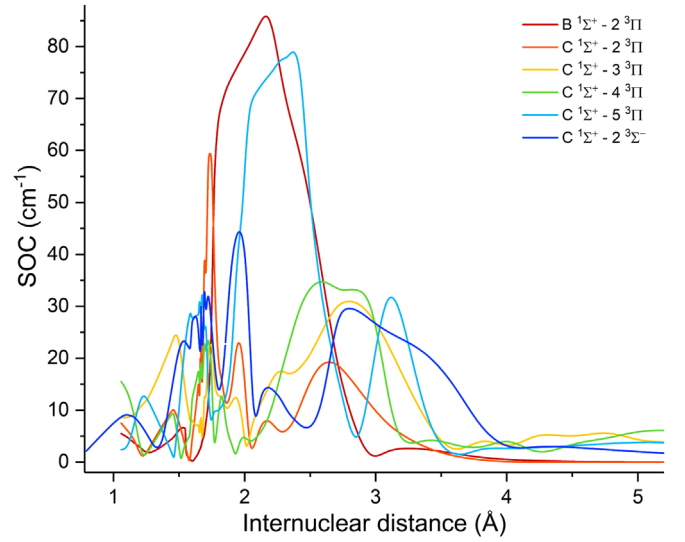


Figure 6. Several important spin-orbit couplings between $^1\Sigma^+$ and $^3\Pi$ states.

Diabatic PECs can be readily transformed back to adiabatic PECs by diagonalizing the diabatic interaction matrix $V(R)$. Adiabatic PECs derived from our diabatic model in this manner should therefore agree with the calculated MRCI+Q energies. To improve our estimates of the diabatic state couplings, we manually refined their values to minimize the differences between the adiabatic energies derived from diagonalizing $V(R)$ and the ab initio energies. The result is shown in Figure 5. The perfect overlap between MRCI+Q data and adiabatic PECs validates our diabaticization process.

We also included states of $^3\Sigma^-$ and $^3\Pi$ symmetry in the coupled-channel model because they have nonvanishing SOC terms with $^1\Sigma^+$ states according to the selection rules:

$$\Delta J = \Delta \Omega = 0; \quad \Delta S = 0, \pm 1; \quad \Sigma^+ \leftrightarrow \Sigma^- \quad (12a)$$

$$\Delta \Lambda = \Delta \Sigma = 0 \text{ or } \Delta \Lambda = -\Delta \Sigma = \pm 1. \quad (12b)$$

In addition, obvious avoided crossings exist between the adiabatic 2, 3, and 4 $^3\Pi$ states, as shown in Figure 2, and these must be included in the model. Diabatic PECs of 2, 3, and 4 $^3\Pi$ states were constructed using the method described above. PECs of the higher-energy 5 and 6 $^3\Pi$ states are not smooth around 1.6 \AA , indicating strong coupling between them that is difficult to incorporate into the diabatic model. However, because both states are dissociative, interactions between them do not affect the overall photodissociation cross section (though they may have a small effect on the atomic product fractions), so we ignore them in our model. No clear crossings occur between the 2, 3 and 4 $^3\Sigma^-$ states, so they are also treated as independent diabatic states in our coupled-channel model.

Finally, we must include the SOCs among these diabatic states. Several important SOCs between the adiabatic states are shown in Figure 6, while all others are given in the Appendix. Because of the complicated adiabatic-to-diabatic transformation of $^1\Sigma^+$ states, it is almost impossible to build R -dependent SOC curves for diabatic states. For this reason we assume that the spin-orbit interaction can be treated as R -independent, and use the values of the SOC matrix elements at the curve crossing points in the CSE model. This is generally a reasonable approximation when two states interact via a curve crossing. For instance, Lewis et al. (2018) used this approach to fit an

	$^1\Sigma^+$				$^3\Pi$						$^3\Sigma^-$			
	A' $^1\Sigma^+$	B' $^1\Sigma^+$	C' $^1\Sigma^+$	3' $^1\Sigma^+$	2 $^3\Pi$	3 $^3\Pi$	4 $^3\Pi$	5 $^3\Pi$	6 $^3\Pi$	2 $^3\Sigma^-$	3 $^3\Sigma^-$	4 $^3\Sigma^-$		
	$^1\Sigma^+$	A' $^1\Sigma^+$	20	0	0	0	6	0	0	0	0	0	0	
B' $^1\Sigma^+$	20		0	200	42	10	20	31	45	17	18	17		
C' $^1\Sigma^+$	0	0		620	6	16	17	40	8	23	15	44		
3' $^1\Sigma^+$	0	200	620		0	0	0	16	17	45	8	52		
$^3\Pi$	2 $^3\Pi$	0	42	6	0		300	150	0	0	0	0		
3 $^3\Pi$	6	10	16	0	300		0	0	0	0	0	0		
4 $^3\Pi$	0	20	17	0	150	0		0	0	0	0	0		
5 $^3\Pi$	0	31	40	16	0	0	0		0	0	0	0		
6 $^3\Pi$	0	45	8	17	0	0	0	0		0	0	0		
$^3\Sigma^-$	2 $^3\Sigma^-$	0	17	23	45	0	0	0	0	0		0		
3 $^3\Sigma^-$	0	18	15	8	0	0	0	0	0	0	0			
4 $^3\Sigma^-$	0	17	44	52	0	0	0	0	0	0	0			

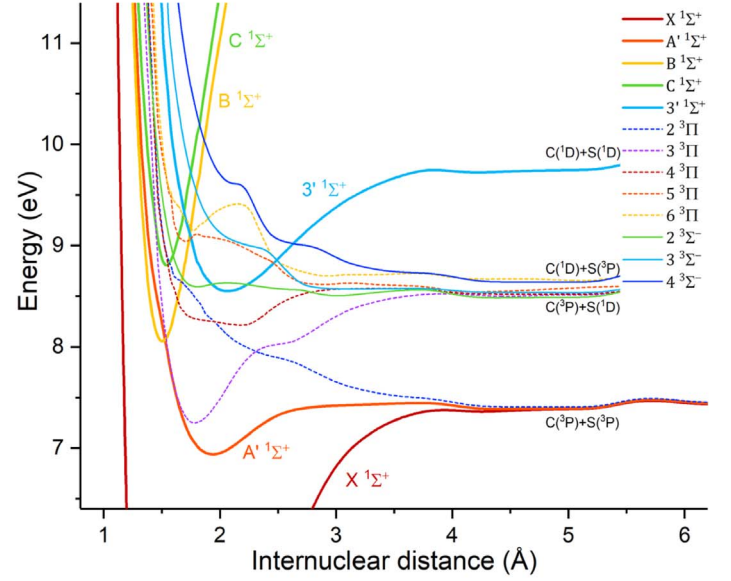


Figure 7. Coupled-channel model built for $^1\Sigma^+$ diatomic states. Left: interaction matrix $V(R)$ off-diagonal elements. Right: PECs of included diatomic states.

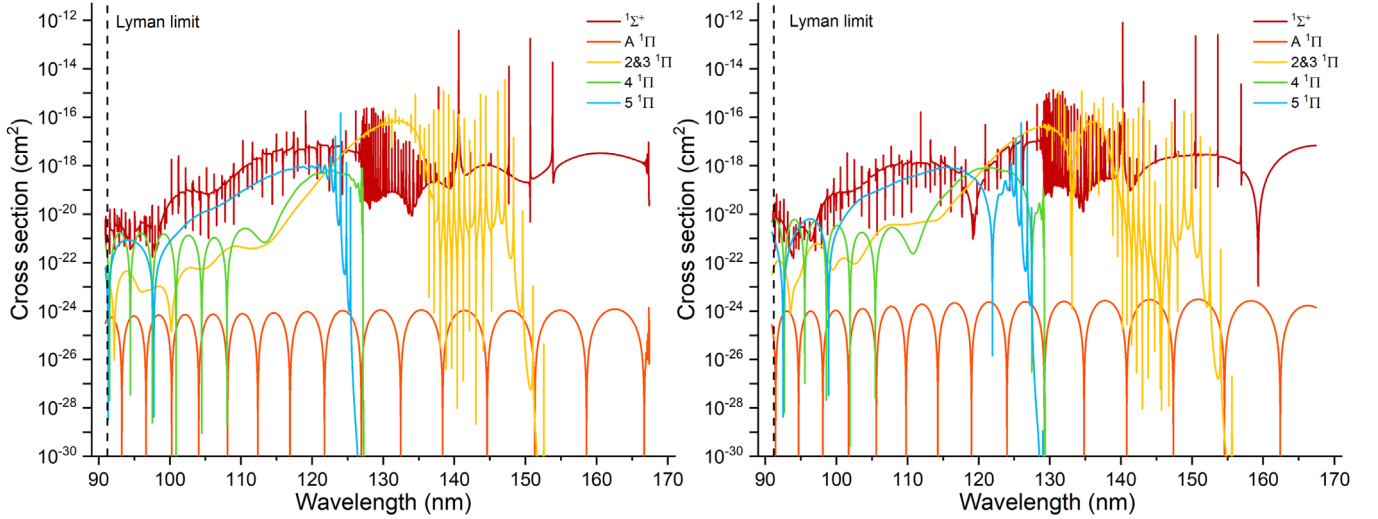


Figure 8. Rotationless photodissociation cross sections of $^1\Sigma^+$ and $^1\Pi$ states, $v'' = 0$ (left) and $v'' = 1$ (right).

R -independent value for the $\langle 1^5\Pi_{u0} | \mathbf{H}^{SO} | B^3\Sigma_{u0}^- \rangle$ matrix element for S_2 to experimental data, obtaining a value within 10% of the ab initio value calculated at the crossing point. Because the crossings between $^3\Pi$ and $^3\Sigma^-$ are at longer internuclear distances and also above the dissociation limits, the couplings between them are unlikely to change the predissociation behavior of $^1\Sigma^+$ states. We therefore do not consider the SOCs between $^3\Pi$ and $^3\Sigma^-$ states in our model. The SOCs are calculated in MOLPRO at the MRCI level, as described in Section 2.1. To convert $\langle 1A_1 | H_{SO} | 3B_1 \rangle$ in the C_{2v} representation into $\langle 1^1\Sigma^+ | H_{SO} | 3^1\Pi \rangle$ in the $C_{\infty v}$ representation, a factor of $\sqrt{2}$ is applied.

The final potentials and coupling matrix for predissociation of the $^1\Sigma^+$ states are shown in Figure 7. The diagonal elements are R -dependent potentials, while the nondiagonal elements represent the R -independent coupling terms.

In addition, when calculating photodissociation cross sections for $^1\Pi$ states, we followed a similar procedure to construct a coupled-channel model for the 2 and 3 $^1\Pi$ states

because they have an obvious crossing at 2.15 Å. Only direct photodissociation is calculated for the A, 4, and 5 $^1\Pi$ states.

3.3. Photodissociation Cross Sections and Rates

From the coupled-channel model of the $^1\Sigma^+$ states, we calculated the rotationless photodissociation cross sections from the $v'' = 0$ and $v'' = 1$ vibrational levels of the ground X electronic state, without taking the Hönl-London factor into consideration. They are shown in Figure 8. The spectroscopic line assignments are listed in Table 4. Predissociation lifetimes τ_{pd} are calculated from the width γ of the peaks (Kirby & Van Dishoeck 1989),

$$\tau_{pd} = \frac{\hbar}{\gamma} = \frac{5.3 \times 10^{-12}}{\gamma}, \quad (13)$$

if τ_{pd} is in s and γ is in cm^{-1} . Spontaneous emission lifetimes τ_{se} are derived from the inverse of the Einstein A coefficients calculated based on the integrated cross sections (σ_0) of these

Table 4
Properties of the $B - X$ and $C - X$ Transitions of CS

Band	$v_{\text{expt}} (\text{cm}^{-1})^a$	$v_{\text{expt}} (\text{cm}^{-1})^b$	$\nu (\text{cm}^{-1})$	$\gamma (\text{cm}^{-1})$	$\sigma_0 (\text{cm}^2 \text{cm}^{-1})$	$\tau_{\text{pd}} (\text{ns})$	$A (\text{s}^{-1})$	$\tau_{\text{se}} (\text{ns})$	
$B - X$	(0 - 0)	64869 ^c	64893 ^c	65011.7	0.50	1.5×10^{-14}	1.1×10^{-2}	4.8×10^7	2.1×10^1
	(1 - 0)	66225 ^c	66225 ^c	66363.7	0.02	5.4×10^{-15}	2.6×10^{-1}	1.8×10^7	5.6×10^1
	(2 - 0)	67560 ^c	...	67718.6	0.02	4.3×10^{-16}	2.6×10^{-1}	1.5×10^6	6.7×10^2
	(1 - 1)	64934 ^d	...	65087.2	0.02	7.8×10^{-15}	2.6×10^{-1}	2.5×10^7	4.0×10^1
$C - X$	(0 - 0)	71388 ^e	71327 ^e	71117.7	0.66	4.0×10^{-13}	8.0×10^{-3}	1.5×10^9	6.6×10^{-1}
	(1 - 0)	72571.5	0.28	8.0×10^{-16}	1.9×10^{-2}	3.2×10^6	3.2×10^2
	(1 - 1)	...	71480 ^e	71295.0	0.28	3.7×10^{-13}	1.9×10^{-2}	1.4×10^9	7.1×10^{-1}

Notes.^a Stark et al. (1987).^b Donovan et al. (1970).^c Band origin.^d Band head position (band origin was not reported).^e Center wavenumber of observed band.**Table 5**Dominant Predissociation Pathways and Product Branching Fractions for the $B - X$ and $C - X$ Transitions of CS

Transition	Band	Channel	Percent	Atomic products
$B - X$	(0 - 0)	$A' \ ^1\Sigma^+$	85.5	$C(^3P) + S(^3P)$
		$2 \ ^3\Pi$	14.5	$C(^3P) + S(^3P)$
	(1 - 0)	$A' \ ^1\Sigma^+$	96.0	$C(^3P) + S(^3P)$
		$2 \ ^3\Pi$	4.0	$C(^3P) + S(^3P)$
		$A' \ ^1\Sigma^+$	95.1	$C(^3P) + S(^3P)$
		$2 \ ^3\Pi$	4.9	$C(^3P) + S(^3P)$
$C - X$	(0 - 0)	$4 \ ^3\Pi$	48.1	$C(^3P) + S(^1D)$
		$5 \ ^3\Pi$	30.9	$C(^3P) + S(^1D)$
		$2 \ ^3\Pi$	11.0	$C(^3P) + S(^3P)$
		$3 \ ^3\Pi$	10.0	$C(^3P) + S(^1D)$
	(1 - 0)	$5 \ ^3\Pi$	35.5	$C(^3P) + S(^1D)$
		$4 \ ^3\Pi$	30.2	$C(^3P) + S(^1D)$
		$2 \ ^3\Sigma^-$	15.1	$C(^3P) + S(^1D)$
		$2 \ ^3\Pi$	11.0	$C(^3P) + S(^3P)$
		$3 \ ^3\Pi$	7.7	$C(^3P) + S(^1D)$

peaks. These values are also included in Table 4 for comparison. From the calculation, we were also able to determine the dominant predissociation pathways for each transition, which are listed in Table 5.

A comparison between the rotationless vibronic transition frequencies derived from our coupled-channel model and the experimental frequencies of Donovan et al. (1970) and Stark et al. (1987) provides strong support for the accuracy of our approach. Our calculated $B - X$ transition frequencies are all slightly greater than the corresponding experimental values by $\sim 150 \text{ cm}^{-1}$, while those of the $C - X$ band are $\sim 200 \text{ cm}^{-1}$ smaller than experimental values. Considering the complexity of this calculation, and the fact that it is purely ab initio with no empirical refinement, the agreement is quite satisfactory.

Line widths of the calculated $B - X$ and $C - X$ cross sections confirm their predissociative nature, especially for the origin band transitions. All the transitions listed in Table 4 can be treated as pure photodissociation lines in the low-density conditions of the ISM because predissociation lifetimes τ_{pd} are much shorter than the spontaneous emission lifetimes τ_{se} . In the experimental VUV spectrum of the $B - X$ transition (Stark et al. 1987), only the (1 - 0) band showed resolvable rotational structure. This matches our calculation, in which the 1 - 0

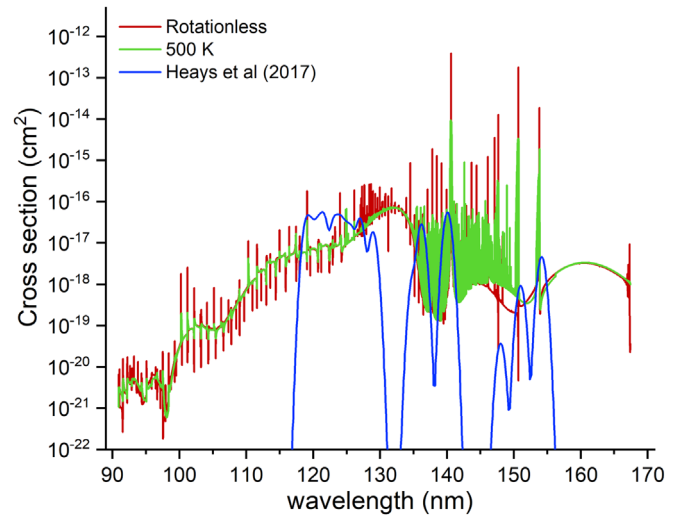


Figure 9. Photodissociation cross sections calculated at LTE temperature 500 K, compared with data adopted in Heays et al. (2017).

transition has the narrowest line width among the three transitions arising from $v'' = 0$. The $C - X$ (0 - 0) transition has the largest cross section among all transitions from $v'' = 0$ considered here by at least a factor of 30 owing to its large TDM and Franck–Condon factor. Its line width of 0.66 cm^{-1} corresponds to $\tau_{\text{pd}} = 8.0 \text{ ps}$, which is over 80 times faster than τ_{se} (0.66 ns).

The CSE method is also able to give the atomic product channels for each transition. For all $B - X$ transitions, the dominant decay pathway is non-adiabatic coupling to the $A' \ ^1\Sigma^+$ state, leading to the ground-state $C(^3P) + S(^3P)$ atomic products. A small percentage ($\sim 15\%$) couples to the $2 \ ^3\Pi$ state via the spin–orbit interaction, but this also leads to the same atomic limit. The ground vibrational level of the C state is calculated to primarily predissociate via the 2, 3, 4 and 5 $^3\Pi$ states by SOCs. Among these, the $2 \ ^3\Pi$ is a minor channel corresponding to the $C(^3P) + S(^3P)$ atomic limit, while all others (representing 89% of the total coupling) give rise to $C(^3P) + S(^1D)$ products.

The photodissociation cross sections from $^1\Pi - X$ transitions are shown in Figure 8.

Rovibronic transitions are then calculated with applying appropriate selection rules and Hönl–London factors. LTE cross

Table 6
CS Photodissociation Rates (s^{-1}) Under the Standard ISRF (Draine 1978)

Source	Rotationless	20 K	100 K	500 K	Pattillo et al. (2018)	Heays et al. (2017)
$B - X$	(0 - 0)	7.03×10^{-11}	7.11×10^{-11}	7.10×10^{-11}	6.82×10^{-11}	...
	(1 - 0)	4.50×10^{-12}	4.41×10^{-11}	3.43×10^{-11}	2.61×10^{-11}	...
	(2 - 0)	8.71×10^{-13}	3.95×10^{-12}	4.15×10^{-12}	3.01×10^{-12}	...
$C - X$	(0 - 0)	1.64×10^{-9}	1.64×10^{-9}	1.64×10^{-9}	1.64×10^{-9}	...
	(1 - 0)	3.24×10^{-12}	3.24×10^{-12}	3.29×10^{-12}	3.58×10^{-12}	...
Remaining ${}^1\Sigma^+ - X$	2.33×10^{-10}	1.95×10^{-10}	2.18×10^{-10}	2.39×10^{-11}
All ${}^1\Sigma^+ - X$	1.96×10^{-9}	1.96×10^{-9}	1.97×10^{-9}	1.98×10^{-9}	1.94×10^{-10}	...
$A {}^1\Pi - X$	6.57×10^{-17}	6.57×10^{-17}	6.61×10^{-17}	6.88×10^{-17}	1.50×10^{-21}	...
2 and 3 ${}^1\Pi - X$	8.84×10^{-10}	8.84×10^{-10}	8.85×10^{-10}	9.07×10^{-10}	1.35×10^{-10}	...
4 ${}^1\Pi - X$	7.14×10^{-12}	7.14×10^{-12}	7.11×10^{-12}	6.96×10^{-12}	4.05×10^{-11}	...
5 ${}^1\Pi - X$	1.54×10^{-11}	1.55×10^{-11}	1.58×10^{-11}	1.62×10^{-11}
All ${}^1\Pi - X$	9.07×10^{-10}	9.06×10^{-10}	9.08×10^{-10}	9.30×10^{-10}	1.76×10^{-10}	...
Total	2.86×10^{-9}	2.87×10^{-9}	2.88×10^{-9}	2.91×10^{-9}	3.70×10^{-10}	9.49×10^{-10}

sections are obtained using the method described in Section 2.2. The LTE cross sections at temperature 500 K are shown in Figure 9. The rotational constant of the $B(v = 1)$ state is calculated to be 0.846 cm^{-1} from the spectrum of the $B - X$ (1 - 0) transition shown in the Appendix, which is almost same as 0.852 cm^{-1} obtained from the measured spectrum (Stark et al. 1987).

By combining the calculated cross sections and the ISRF (Draine 1978), the total photodissociation rate of CS at different temperatures are shown in Table 6, compared with the results obtained by Pattillo et al. (2018) and the standard values in the Leiden photodissociation database (Heays et al. 2017). The dominant transition responsible for the photodissociation of CS in space is the $C - X$ (0 - 0) band, comprising about 57% of the total photodissociation in the rotationless case. Dissociation through ${}^1\Pi$ states contributes about 32% to the overall rate. Our calculated rate is a factor of 7.7 larger than that calculated by Pattillo et al. (2018) and a factor of about 3.0 larger than the value adopted by Heays et al. (2017).

At higher energies, Donovan et al. (1970) identified three bands at 122.93, 121.10, and 121.91 nm, which were in turn tentatively assigned as the $G {}^1\Pi - X$ (0-0) and (1-0) transitions as well as a forbidden transition. Because these transitions occur near $\text{Ly}\alpha$, they may provide important contributions to the total CS photodissociation rate in regions where $\text{Ly}\alpha$ is dominant. Our calculations do not show bands that match those reported in the 122 nm region. The calculated ${}^1\Sigma^+$ states show a smooth cross section due to direct photodissociation in this region, and while the 4 and 5 ${}^1\Pi$ states show large direct cross sections around 121.6 nm, they are still about one order of magnitude lower than the values given in the Leiden database. The lack of discrete bands around 122 nm is likely due to the limited number of states in the MRCI calculation and perhaps also due to the limited number of π orbitals included in the active space. While we were able to calculate electronic energies in this range for both ${}^1\Sigma$ and ${}^1\Pi$ states, the PECs were not smooth and continuous. Therefore only direct photodissociation from lower excited states was calculated in the 122 nm energy range. Consequently, our cross sections are expected to be highly uncertain in the $\text{Ly}\alpha$ region. In addition, it should be noted that the cross sections in the Leiden photodissociation database (Heays et al. 2017) are also highly uncertain in this same region, so additional work is

needed to address the potential importance of CS photodissociation by $\text{Ly}\alpha$.

4. Conclusion

Here we have presented a detailed ab initio theoretical study of CS photodissociation from its ground electronic state using PECs calculated with the MRCI+Q method with a custom basis set derived from aug-cc-pV(5+d)Z with additional diffuse functions. To improve the quality of the calculation for high-lying excited states, especially for the $B {}^1\Sigma^+$ and $C {}^1\Sigma^+$ states that have known strong predissociative bands from previous experiments, an expanded active space including more Rydberg MOs was used. Our calculation yields spectroscopic constants for the ground X and several low-lying excited electronic states in excellent agreement with experimental data.

Photodissociation cross sections were calculated using coupled-channel models for excited states from the ab initio calculation, considering both non-adiabatic and SOCs. By combining these cross sections with the ISRF, CS photodissociation rates were derived at a variety of LTE temperatures along with the dominant atomic product channels. In space, the dominant photodissociation process for CS occurs through the $C - X$ transition followed by SOC to several ${}^3\Pi$ and ${}^3\Sigma^-$ states, yielding C atoms in the ground 3P state and S atoms in the metastable 1D state. Compared with other estimates of CS photodissociation, we obtain a rate that is a factor of 3.0 larger than that adopted by the Leiden database (Heays et al. 2017). Our rates are about a factor of 7.7 greater than those estimated in the recent calculation of Pattillo et al. (2018), arising from the fact that their choice of active space provided an inadequate treatment of Rydberg ${}^1\Sigma^+$ states that have strong transitions from the ground electronic state.

Finally, we would like to give an overall estimate of the accuracy of our results. The foundation of our photodissociation cross sections and rates is the PECs and TDMs obtained from the ab initio MRCI+Q calculation, which is judged to be highly reliable by all available spectroscopic data. Transition line widths derived from the CSE calculation show that the $B - X$ and $C - X$ transitions can be considered completely dissociative in low-density environments where collisional relaxation is unavailable. Uncertainties in the magnitudes of the couplings between states may shift the calculated transition frequencies and line widths somewhat; however, these factors should have a minimal effect on the total calculated cross

sections, which are mainly determined by the TDMs and Franck–Condon factors. Previous studies of diatomic molecules have shown that cross sections derived from high-level ab initio calculations such as those employed here are generally accurate to within 20%. We have confidence that the cross sections calculated for the $B - X$ and $C - X$ bands have similar accuracy.

We found that the $C - X (0 - 0)$ transition is responsible for 57% of the overall photodissociation of CS under the standard ISRF. This is expected when compared with photodissociation of CO because CS has a lower dissociation energy and a substantially higher density of electronic states allowing for ample opportunities for predissociation. While our transition frequencies differ from experimental values by about 200 cm^{-1} , our computed rates should be reliable as long as the radiation field is smooth in the vicinity of 140 nm. The atomic product branching fractions are more uncertain because their values are sensitive to the exact methods used in the diabaticization procedure. Future high-resolution spectroscopic measurements of the $B - X$ and $C - X$ bands, along with atomic branching ratios, would provide a good test for judging the ultimate accuracy of these calculations. They would also lead to improvements in the derived cross sections and rates because the experimentally measured energy levels can be used to improve the diabaticization and refine the ab initio PECs.

Nevertheless, our calculations still have some limitations. First, while we proved that several low-lying vibrational states of the B and C electronic states are totally predissociative, the same may not be true for higher vibrational states. Second, we are less confident in the accuracy of our electronic states at energies above the C state. In our model, the dominant contribution to the cross section below ~ 130 nm is direct photodissociation via the $^1\Sigma^+$ states. The direct photodissociation cross section in this region for the states included in our calculation should be reliable to $\sim 20\%$, limited primarily by the accuracy of the TDMs. However, several higher $^1\Sigma^+$ and $^1\Pi$ states with energies below the Lyman limit exist and should also contribute somewhat to the total photodissociation, although their TDMs with the ground vibronic state are likely much smaller than the $C - X (0 - 0)$ band. These states will likely make a significant contribution to the total cross section via direct photodissociation, and so our calculated cross section in this region should be taken as a lower limit. Although any predissociation from higher-energy states would make only a small contribution to the total photodissociation rate in a smooth radiation field (much less than 10%), previous experiments (Donovan et al. 1970) have indicated the presence of such a state near 121.6 nm. Because our ab initio data and CSE calculations do not cover this energy range adequately, we do not attempt to calculate the CS photodissociation rate by Ly α radiation, and this is an area in need of future investigation.

This work was supported by the NASA Astrophysics Research and Analysis program under awards 80NSSC18K0241 and 80NSSC19K0303.

Appendix Additional Data and Figures

To verify convergence, we calculated the potential energy at several points for a series of basis sets, including aug-cc-pVQZ, aug-cc-pV5Z, aug-cc-pV6Z, aug-cc-pV(Q+d)Z with Rydberg diffuse functions, and finally aug-cc-pV(5+d)Z with Rydberg

diffuse functions, which was used for the final calculations in the present study. The exponents of the additional Rydberg diffuse functions are shown in Table 1. The PECs of the X , A' , B , C , and A states are shown in Figure 10 after subtracting the energy of the X state at $R = 1.542 \text{ \AA}$. Inclusion of additional Rydberg diffuse functions lowers the energy of the B state significantly. A maximum error of 0.08 eV can be estimated for the B state from the difference between calculations with aug-cc-pV6Z and aug-cc-pV(5+d)Z with Rydberg diffuse functions. The A' , C , and A states are well converged.

The PECs of all calculated states obtained from the SA-CASSCF/MRCI+Q calculations described in Section 2.1 are given in Table 7. Blank entries in the table indicate that the calculation did not converge at a particular value of R or that the state fell outside the range of those calculated for a particular symmetry. Of these 49 electronic states, the PECs of 21 states are shown in Figure 2, while the PECs of an additional 24 states are shown in Figure 11. The data for the remaining 4 states, $7^1\Sigma^+$, $3^1\Sigma^-$, $7^1\Pi$, and $4^3\Sigma^+$, are not shown, but are available in Table 7.

The absolute values of the TDMs between $^1\Sigma^+$ and $^1\Pi$ states and the ground $X^1\Sigma^+$ state are shown in Table 8. Like in Table 7, blank entries indicate convergence failure or that the particular state was not calculated at the indicated R value. Additionally, the SOCs between the $^1\Sigma^+$, $^3\Sigma^-$, and $^3\Pi$ states that are not already shown in Figure 6 are presented in Figure 12.

When we calculated the photodissociation cross sections for $^1\Pi$ states, we built a coupled-channel model to treat the $2^1\Pi$ and $3^1\Pi$ states. The interaction matrix is shown in Figure 13. We ignored any couplings involving $4^1\Pi$ and $5^1\Pi$ states because their interactions are subtle and not obvious. This may introduce errors into cross-section calculations in the energy range near these states.

The TDMs were diabaticized along with the PECs by exchanging the values on both sides of the crossing points, and they are shown in Figure 14. Because diabatic PECs of the B and C states at longer internuclear distances were built by shifting PECs of the $\text{CS}^+ X$ state, we manually reduced the TDMs of these two diabatic states to 0 in this region. As before, we ignored any couplings involving the $4^1\Pi$ and $5^1\Pi$ states. The wavefunction of the $X (v = 0, J = 0)$ state is also plotted to indicate the Franck–Condon region. The diabatic PECs and corresponding TDMs used in the coupled-channel cross-section calculation are available in Table 9.

The rotationless cross sections of photodissociation from $X^1\Sigma^+ v'' = 0, 1$ are given in Tables 10 and 11. The calculation was performed with 1 cm^{-1} resolution between 59,732 and $110,000 \text{ cm}^{-1}$, with additional points using smaller steps around several $B - X$ and $C - X$ transitions to better resolve the line shapes near bound–bound transitions. LTE cross sections at various temperatures are shown in Table 12. These values were calculated using Equation (6) by summing over the photodissociation cross sections for the following rotational and vibrational levels of the CS ground X state: $J'' = 0-53$ of $v'' = 0$, $J'' = 0-51$ of $v'' = 1$, and $J'' = 0-43$ of $v'' = 2$. These lower states were chosen so that cross sections at temperatures up to 500 K can be derived accurately. Owing to the increased line density at elevated temperatures, the grid size for each temperature was adapted based on the peak positions. The final wavenumber grid is a collection of all the wavenumbers used. Linear spline interpolation was used to generate estimated values at other small-step wavenumbers that were not explicitly calculated.

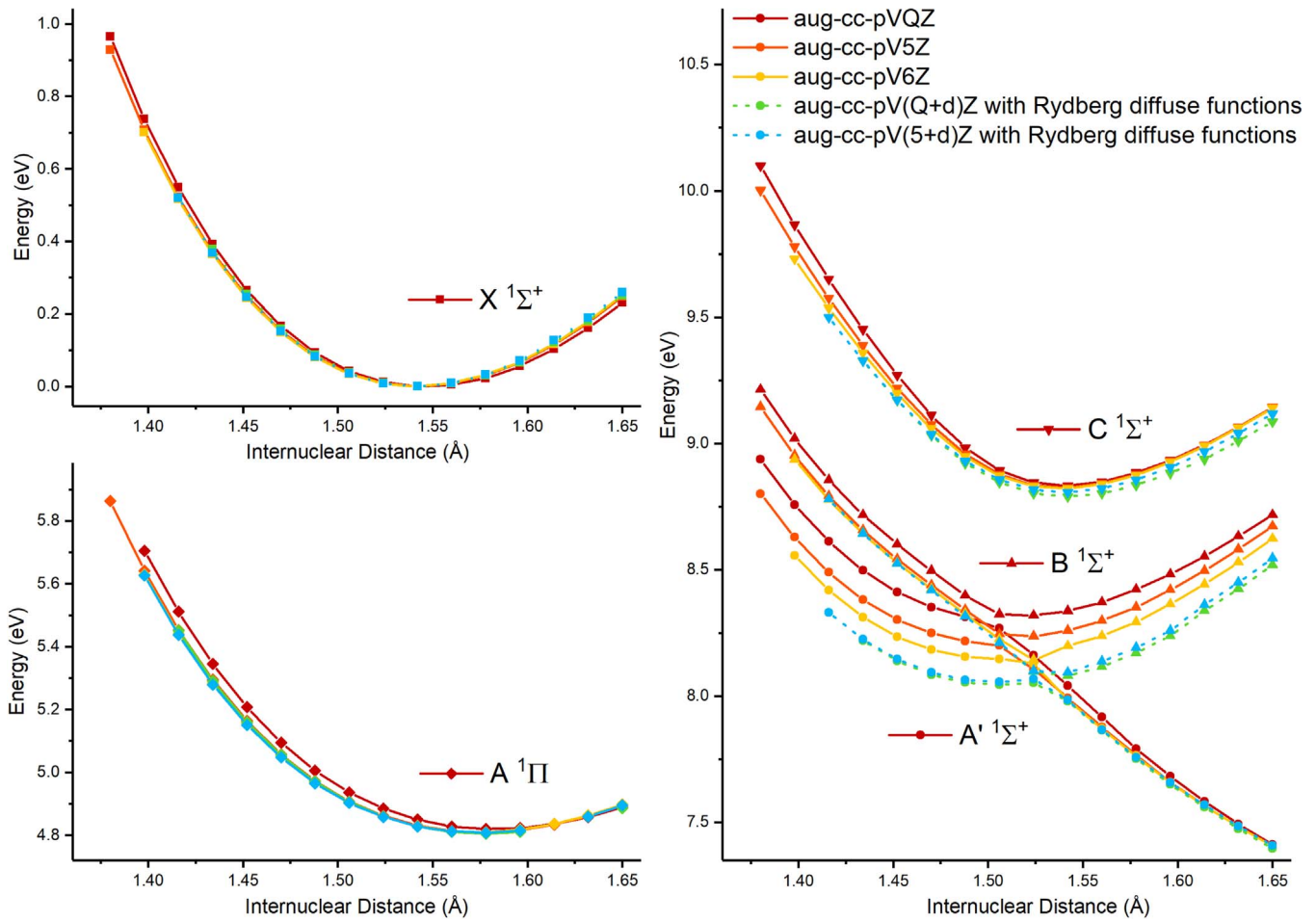


Figure 10. Potential energy curves of several states calculated with a series of basis sets.

Table 7
MRCI+Q/aug-cc-pV(5+d)Z PECs for All Electronic States of CS

R (Å)	$1^1\Sigma^+$	$2^1\Sigma^+$	$3^1\Sigma^+$	$4^1\Sigma^+$	$5^1\Sigma^+$	$6^1\Sigma^+$	$7^1\Sigma^+$	$1^1\Sigma^-$...	$1^5\Delta$
0.7938	74.87140	78.93278	79.66499	80.30997	80.72843	80.83307	86.83185
0.8996	43.05554	48.49688	49.24178	50.00352	50.40615	53.09136	55.71249	59.76372
0.9261	53.68723
0.9525	31.91984	37.79983	38.51802	39.24516	39.51339	42.98093	44.81884	48.29292
...
7.6731	7.47457	7.48510	9.83764	9.85174	9.88433	7.48108	...	7.48958
7.9377	7.47481	7.48548	9.83861	9.85228	9.88486	7.48135	...	7.48967

Note.

^a PECs are in eV.

(This table is available in its entirety in machine-readable form.)

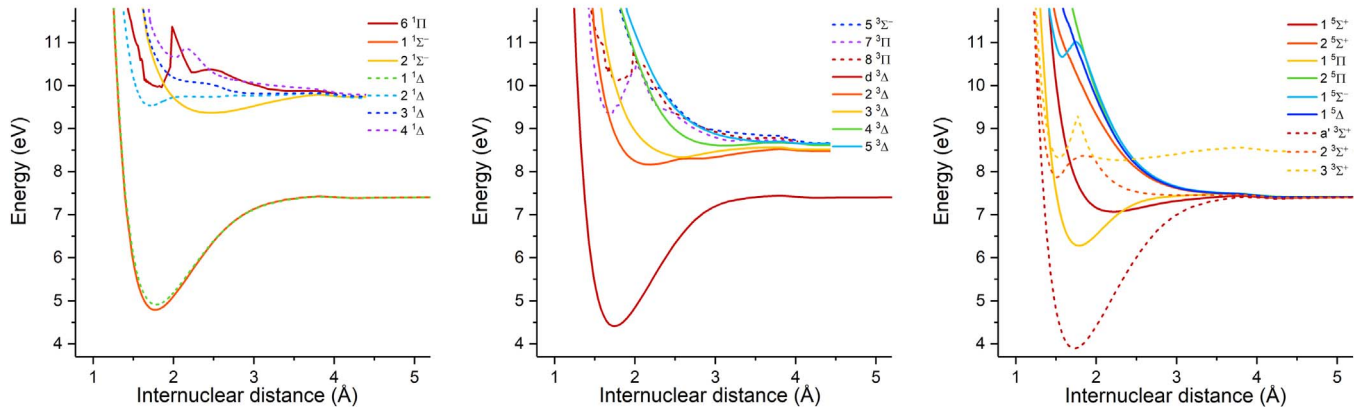


Figure 11. Potential energy curves of the remaining electronic states of CS.

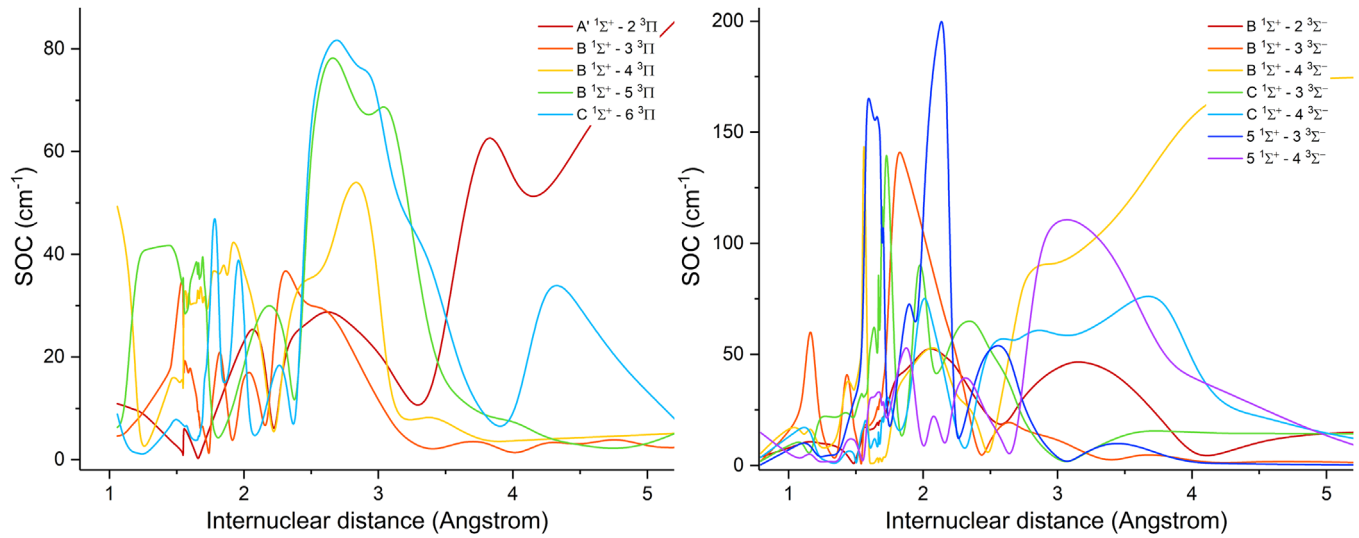


Figure 12. Several spin-orbit couplings between electronic states of CS.

Table 8
TDMs between $1\Sigma^+$ and 1Π States and the Ground Electronic State $X\ 1\Sigma^+$

R (Å)	$2\ 1\Sigma^+$	$3\ 1\Sigma^+$	$4\ 1\Sigma^+$	$5\ 1\Sigma^+$	$6\ 1\Sigma^+$	$7\ 1\Sigma^+$	$1\ 1\Pi$...	$7\ 1\Pi$
0.7938	0.86039	1.19859	0.36731	0.53697	0.08515	0.19403	0.30781	...	0.12908
0.8996	0.44859	0.83099	0.35651	0.75145	0.06795	0.42810
0.9525	0.34744	0.66844	0.26586	0.90374	0.08933	0.47362
1.0584	0.12811	0.63043	0.01976	0.81387	0.07418	0.52310	0.14462	...	0.40322
...
7.6731	0.00005	0.00000	0.00000	0.00000	0.00039
7.9377	0.00003	0.00000	0.00000	0.00000	0.00034

Note.

^a TDMs are in atomic units.

(This table is available in its entirety in machine-readable form.)

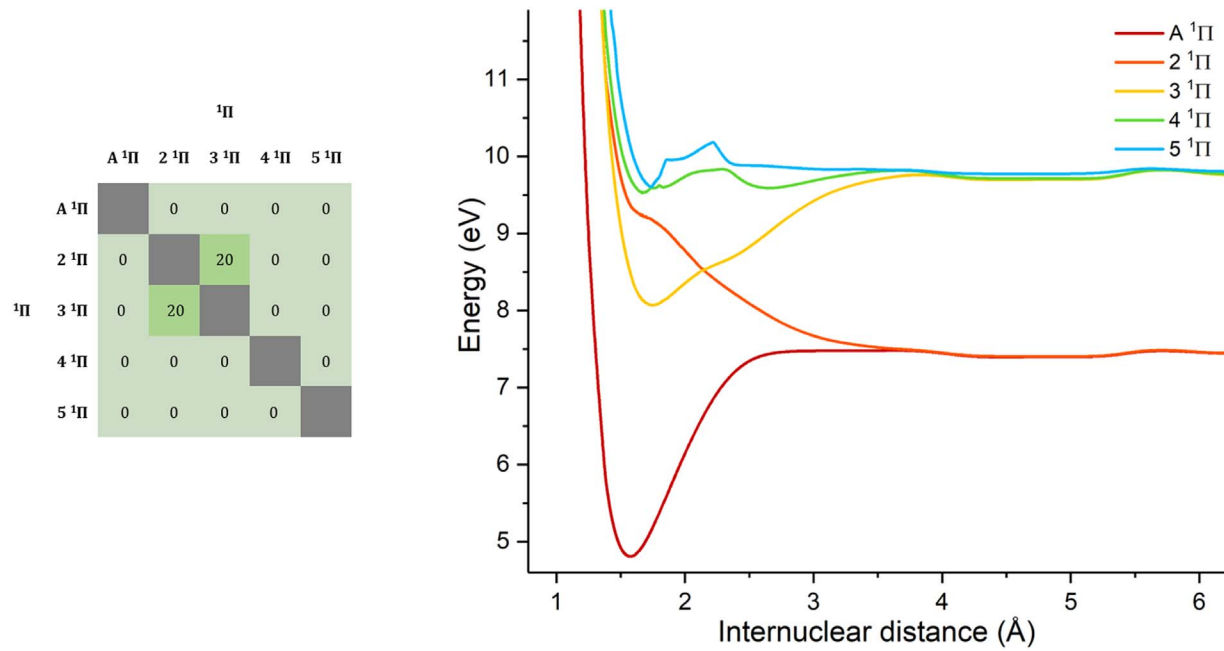


Figure 13. Coupled-channel model for the ${}^1\Pi$ diabatic states. Left: interaction matrix $V(R)$ off-diagonal elements, in cm^{-1} . Right: PECs of included diabatic states.

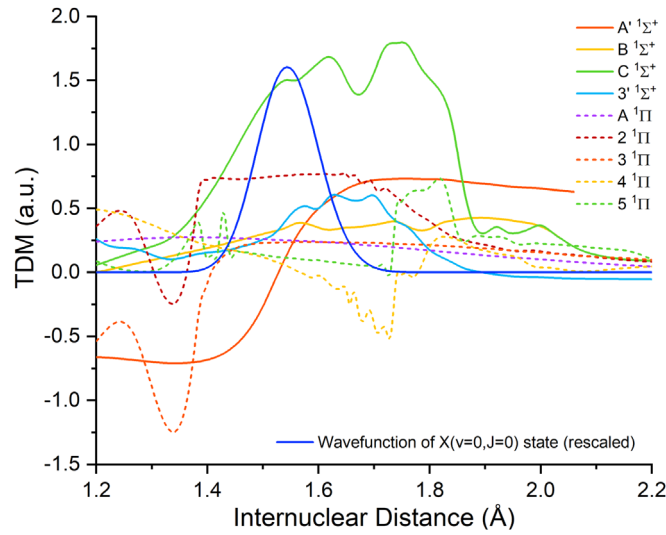


Figure 14. TDMs for diabatic states from the ground X state.

Table 9
PECs and TDMs of Diabatic Model Built for CS

R (Å)	pec- $X\ ^1\Sigma^+$	pec- $A'\ ^1\Sigma^+$	pec- $B\ ^1\Sigma^+$	pec- $C\ ^1\Sigma^+$	pec- $3'\ ^1\Sigma^+$	pec- $2\ ^3\Pi$	pec- $3\ ^3\Pi$...	tdm- $5\ ^1\Pi$
1.050	17.7367	24.8385	24.1887	25.8028	30.7668	30.6747	27.3703	...	0.197
1.052	17.5116	24.6238	23.9754	25.5914	30.5403	30.4289	27.1524	...	0.185
1.054	17.2886	24.4113	23.7642	25.3820	30.3157	30.1857	26.9367	...	0.174
1.056	17.0677	24.2009	23.5552	25.1745	30.0930	29.9450	26.7230	...	0.162
⋮	⋮	⋮	⋮	⋮	⋮	⋮	⋮	⋮	⋮
7.796	7.4748	7.4854	14.4318	15.1823	9.8381	7.4935	8.5675	...	0.000
7.798	7.4748	7.4854	14.4318	15.1823	9.8381	7.4935	8.5675	...	0.000

Notes.

^a PECs are in eV.

^b TDMs are in atomic units.

(This table is available in its entirety in machine-readable form.)

Table 10
Rotationless Photodissociation Cross Sections from the $X^1\Sigma^+ v'' = 0$ Level of CS

$\tilde{\nu}$ (cm ⁻¹)	All $^1\Sigma^+$	1 $^1\Pi$	2 and 3 $^1\Pi$	4 $^1\Pi$	5 $^1\Pi$	Total
59732.000	3.51e-20	3.10e-25	1.79e-96	0.00e+00	0.00e+00	3.51e-20
59733.000	3.66e-20	4.12e-25	9.93e-97	0.00e+00	0.00e+00	3.66e-20
59734.000	3.28e-20	7.76e-26	7.44e-97	0.00e+00	0.00e+00	3.28e-20
59735.000	2.96e-20	3.20e-26	6.55e-97	0.00e+00	0.00e+00	2.96e-20
⋮	⋮	⋮	⋮	⋮	⋮	⋮
109998.000	1.75e-21	3.09e-25	3.21e-23	6.15e-22	6.38e-23	2.46e-21
109999.000	1.40e-21	3.08e-25	3.21e-23	6.16e-22	6.40e-23	2.11e-21

Note.^a Cross sections are in cm².

(This table is available in its entirety in machine-readable form.)

Table 11
Rotationless Photodissociation Cross Sections from the $X^1\Sigma^+ v'' = 1$ Level of CS

$\tilde{\nu}$ (cm ⁻¹)	All $^1\Sigma^+$	1 $^1\Pi$	2 and 3 $^1\Pi$	4 $^1\Pi$	5 $^1\Pi$	Total
59732.000	6.83e-18	1.40e-24	2.19e-71	0.00e+00	0.00e+00	6.83e-18
59733.000	6.83e-18	1.40e-24	2.25e-71	0.00e+00	0.00e+00	6.83e-18
59734.000	6.83e-18	1.40e-24	2.30e-71	0.00e+00	0.00e+00	6.83e-18
59735.000	6.83e-18	1.40e-24	2.36e-71	0.00e+00	0.00e+00	6.83e-18
⋮	⋮	⋮	⋮	⋮	⋮	⋮
109998.000	5.19e-21	2.72e-25	3.18e-23	4.67e-21	1.82e-21	1.17e-20
109999.000	5.19e-21	2.73e-25	3.18e-23	4.66e-21	1.82e-21	1.17e-20

Note.^a Cross sections are in cm².

(This table is available in its entirety in machine-readable form.)




Table 12
LTE Photodissociation Cross Sections for Ground-state CS

$\tilde{\nu}$ (cm ⁻¹)	20 K	50 K	100 K	500 K
59732.000	1.17e-19	4.34e-19	6.71e-19	9.99e-19
59733.000	1.42e-19	4.95e-19	7.24e-19	1.02e-18
59734.000	1.78e-19	5.88e-19	8.10e-19	1.04e-18
59735.000	1.91e-19	6.18e-19	8.36e-19	1.05e-18
⋮	⋮	⋮	⋮	⋮
109998.000	2.28e-21	1.76e-21	1.40e-21	9.78e-22
109999.000	1.55e-21	1.13e-21	8.74e-22	5.53e-22

Note.^a Cross sections are in cm².

(This table is available in its entirety in machine-readable form.)

ORCID iDs

Zhongxing Xu  <https://orcid.org/0000-0003-3815-7647>
 S. R. Federman  <https://orcid.org/0000-0002-8433-9663>
 William M. Jackson  <https://orcid.org/0000-0002-1961-9466>
 Cheuk-Yiu Ng  <https://orcid.org/0000-0003-4425-5307>
 Lee-Ping Wang  <https://orcid.org/0000-0003-3072-9946>
 Kyle N. Crabtree  <https://orcid.org/0000-0001-5629-5192>

References

Asplund, M., Grevesse, N., Sauval, A. J., & Scott, P. 2009, *ARA&A*, **47**, 481
 Baer, M. 2006, *Beyond Born–Oppenheimer: Conical Intersections and Electronic Non-Adiabatic Coupling Terms* (Hoboken, NJ: Wiley)

Barrow, R., Dixon, R., Lagerqvist, A., & Wright, C. 1960, *Arkiv Foer Fysik*, **18**, 543
 Bell, S., Ng, T. L., & Suggitt, C. 1972, *JMoSp*, **44**, 267
 Bruna, P. J., Kammer, W. E., & Vasudevan, K. 1975, *CP*, **9**, 91
 Canaves, M. V., de Almeida, A. A., Boice, D. C., & Sanzovo, G. C. 2007, *AdSpR*, **39**, 451
 Carlson, T. A., Copley, J., Durić, N., Erman, P., & Larsson, M. 1979, *CP*, **42**, 81
 Coppens, P., & Drowart, J. 1995, *CPL*, **243**, 108
 Cossart, D., & Bergeman, T. 1976, *JChPh*, **65**, 5462
 Crawford, F. H., & Shurcliff, W. A. 1934, *PhRv*, **45**, 860
 Destree, J. D., Snow, T. P., & Black, J. H. 2009, *ApJ*, **693**, 804
 Donovan, R. J., Husain, D., & Stevenson, C. D. 1970, *Trans. Faraday Soc.*, **66**, 1
 Draine, B. T. 1978, *ApJS*, **36**, 595
 Drdla, K., Knapp, G. R., & van Dishoeck, E. F. 1989, *ApJ*, **345**, 815
 Druard, C., & Wakelam, V. 2012, *MNRAS*, **426**, 354
 Dunning, T. H., Peterson, K. A., & Wilson, A. K. 2001, *JChPh*, **114**, 9244
 Dunning, T. H., Jr., & Hay, P. J. 1977, in *Methods of Electronic Structure Theory*, ed. H. F. Schaefer (Boston, MA: Springer), 1
 Federman, S. R., Fritts, M., Cheng, S., et al. 2001, *ApJS*, **134**, 133
 Field, R. W., & Bergeman, T. H. 1971, *JChPh*, **54**, 2936
 Gauyacq, D., & Horani, M. 1978, *CaJPh*, **56**, 587
 Gibson, S. 2016, *Pydiatomic: Pydiatomic Initial Release v0.1-alpha*, Zenodo, doi:10.5281/zenodo.56871
 Gibson, S. T., & Lewis, B. R. 1996, *JESRP*, **80**, 9
 Hansson, A., & Watson, J. K. 2005, *JMoSp*, **233**, 169
 Heays, A. N. 2010, PhD thesis, Australian National Univ.
 Heays, A. N., Bosman, A. D., & van Dishoeck, E. F. 2017, *A&A*, **602**, A105
 Heays, A. N., Lewis, B. R., Gibson, S. T., Stark, G., & de Oliveira, N. 2015, *EPJWC*, **84**, 03004
 Heithausen, A., Corneliussen, U., & Grossmann, V. 1998, *A&A*, **330**, 311
 Huber, K. P., & Herzberg, G. 1979, *Molecular Spectra and Molecular Structure* (Boston, MA: Springer)
 Jackson, W. M., Halpern, J. B., Feldman, P. D., & Rahe, J. 1982, *A&A*, **107**, 385
 Johnson, B. R. 1978, *JChPh*, **69**, 4678
 Kendall, R. A., Dunning, T. H., & Harrison, R. J. 1992, *JChPh*, **96**, 6796

- Kewley, R., Sastry, K. V. L. N., Winnemissner, M., & Gordy, W. 1963, *JChPh*, **39**, 2856
- Kirby, K. P., & Van Dishoeck, E. F. 1989, *Advances in Atomic and Molecular Physics*, Vol. 25 (Amsterdam: Elsevier), 437
- Knowles, P. J., & Werner, H.-J. 1985, *CPL*, **115**, 259
- Knowles, P. J., & Werner, H.-J. 1988, *CPL*, **145**, 514
- Knowles, P. J., & Werner, H.-J. 1992, *AcTC*, **84**, 95
- Lefebvre-Brion, H., & Field, R. W. 2004, *The Spectra and Dynamics of Diatomic Molecules* (Amsterdam: Elsevier)
- Lewis, B. R., Gibson, S. T., Hawes, F. T., & Torop, L. W. 2001, *PCEC*, **26**, 519
- Lewis, B. R., Gibson, S. T., Stark, G., & Heays, A. N. 2018, *JChPh*, **148**, 244303
- Li, R., Wei, C., Sun, Q., et al. 2013, *JPCA*, **117**, 2373
- Loison, J.-C., Halvick, P., Bergeat, A., Hickson, K. M., & Wakelam, V. 2012, *MNRAS*, **421**, 1476
- Lovas, F. J., & Krupenie, P. H. 1974, *JPCRD*, **3**, 245
- Lucas, R., & Liszt, H. S. 2002, *A&A*, **384**, 1054
- Mahon, C. A., Stampanoni, A., Luque, J., & Crosley, D. R. 1997, *JMoSp*, **183**, 18
- McQuinn, K. B. W., Simon, R., Law, C. J., et al. 2002, *ApJ*, **576**, 274
- Mockler, R. C., & Bird, G. R. 1955, *PhRv*, **98**, 1837
- Ornellas, F. R. 1998, *CPL*, **296**, 25
- Pattillo, R. J., Cieszewski, R., Stancil, P. C., et al. 2018, *ApJ*, **858**, 10
- Penzias, A. A., Solomon, P. M., Wilson, R. W., & Jefferts, K. B. 1971, *ApJL*, **168**, L53
- Scappini, F., Cecchi-Pestellini, C., Casu, S., & Olberg, M. 2007, *A&A*, **466**, 243
- Semenov, D., Favre, C., Fedele, D., et al. 2018, *A&A*, **617**, A28
- Shi, D., Niu, X., Sun, J., & Zhu, Z. 2013, *JChPh*, **139**, 044306
- Stark, G., Yoshino, K., & Smith, P. L. 1987, *JMoSp*, **124**, 420
- Taylor, G. W., Setser, D. W., & Coxon, J. A. 1972, *JMoSp*, **44**, 108
- Tearson, A., & Palmer, H. B. 1968, *JMoSp*, **27**, 246
- Trabelsi, T., Al-Mogren, M. M., Hochlaf, M., & Francisco, J. S. 2018, *JChPh*, **149**, 064304
- van der Tak, F. F. S., Boonman, A. M. S., Braakman, R., & van Dishoeck, E. F. 2003, *A&A*, **412**, 133
- van Dishoeck, E. F., van Hemert, M. C., Allison, A. C., & Dalgarno, A. 1984, *JChPh*, **81**, 5709
- Vidal, T. H. G., Loison, J.-C., Jaziri, A. Y., et al. 2017, *MNRAS*, **469**, 435
- Wakelam, V., Hersant, F., & Herpin, F. 2011, *A&A*, **529**, A112
- Watson, J. K. G. 2008, *JMoSp*, **252**, 5
- Werner, H.-J., & Knowles, P. J. 1985, *JChPh*, **82**, 5053
- Werner, H.-J., & Knowles, P. J. 1988, *JChPh*, **89**, 5803
- Werner, H.-J., Knowles, P. J., Knizia, G., et al. 2015, MOLPRO, Version 2015.1, a Package of Ab Initio Programs
- Werner, H.-J., Knowles, P. J., Knizia, G., Manby, F. R., & Schütz, M. 2012, *WIREs Comput. Mol. Sci.*, **2**, 242
- Yurchenko, S. N., Lodi, L., Tennyson, J., & Stolyarov, A. V. 2016, *CoPhC*, **202**, 262
- Zuckerman, B., Morris, M., Palmer, P., & Turner, B. E. 1972, *ApJL*, **173**, L125